Exact theory of three-dimensional flow separation. Part 1. Steady separation

By A. S U R A N A, O. G R U N B E R G and G. H A L L E R

Department of Mechanical Engineering, Massachusetts Institute of Technology, 77 Massachusetts Ave., Rm. 3-352, Cambridge, MA 02139, USA
ghaller@mit.edu

We derive an exact theory of three-dimensional steady separation and reattachment using nonlinear dynamical systems methods. Specifically, we obtain criteria for separation points and separation lines on fixed no-slip boundaries in compressible flows. These criteria imply that there are only four basic separation patterns with well-defined separation surfaces. We also derive a first-order prediction for the separation surface using wall-based quantities; we verify this prediction using flow models obtained from local expansions of the Navier–Stokes equations.

1. Introduction

In this paper, we develop a rigorous theory of three-dimensional steady flow separation on no-slip boundaries at rest. We view flow separation as the detachment of fluid from the boundary, a process that results either in small-scale recirculation or large-scale boundary-layer separation. The theory presented here covers general compressible velocity fields that are continuously differentiable and mass-conserving along the boundary.

1.1. *Prior work on three-dimensional steady separation*

Prandtl (1904) showed that a two-dimensional steady flow separates from a no-slip boundary at isolated points where the wall shear (skin friction) vanishes and admits a negative gradient. By contrast, numerical simulations and experiments show three-dimensional flows to separate along lines, not isolated skin-friction zeros (see Tobak & Peake 1982; Chapman 1986; Simpson 1996; and Délery 2001 for reviews).

The most prominent on-wall signature of three-dimensional separation is the skin-friction distribution it generates. Legendre (1956) proposed analysing such distributions using the geometric theory of two-dimensional smooth vector fields. In such an analysis, one locates zeros (critical points) of the skin-friction field, identifies their stability type, then constructs the phase portrait of skin-friction trajectories. This critical-point-based local approach to three-dimensional separation was adopted and refined by several authors (e.g. Perry & Fairlie 1974; Hunt *et al.* 1978; Dallmann 1983; and Yates & Chapman 1992; see Délery 2001 for further references).

Taking a more global view, Lighthill (1963) proposed that convergence of skin-friction lines is a necessary criterion for separation. He went on to deduce that separation lines always start from saddle-type skin-friction zeros and terminate at stable spirals or nodes. Ever since, this heuristic separation criterion has been helpful in interpreting a number of separated flow phenomena (see Délery 2001 for a comprehensive list).

Subsequently, topology and dynamical systems theory were applied in several studies to analyse skin-friction patterns. Notably, Hunt *et al.* (1978) obtained topological constraints on the number and type of singular points on three-dimensional bodies. Peake & Tobak (1981) invoked structural stability and bifurcations to describe changes in skin-friction patterns under varying flow conditions.

Meanwhile, Wang (1972, 1974) challenged Lighthill's separation criterion with examples where none of the converging skin-friction lines originate from saddles. Wang termed the resulting separation open (the separation line starts or ends away from skin-friction zeros), as opposed to Lighthill's closed separation paradigm (the separation line connects skin-friction zeros). Initially contentious, open separation has gradually gained recognition after further numerical and experimental confirmation (Tobak & Peake 1982; Yates & Chapman 1992).

As a new development, Wu, Gu & Wu (1987) moved beyond skin-friction patterns and viewed separation as distinguished three-dimensional particle motion near the boundary. They defined the separation surface as a two-dimensional set of fluid trajectories backward-asymptotic to a saddle-type skin-friction zero. This appears to be the first suggestion that separation surfaces are unstable manifolds in the sense of nonlinear dynamics (see, e.g. Guckenheimer & Holmes 1983).

For the boundary layer equations, Van Dommelen & Cowley (1990) also advocated the particle-based (Lagrangian) view of separation, with a primary focus on unsteady flows. They proposed that the Jacobian of particle positions with respect to their initial positions becomes singular at separation. Such singularities are absent in physical flows, but material spike formation is indeed a well-documented signature of separation.

More recently, Wu *et al.* (2000) derived conditions for the simultaneous convergence and upwelling of fluid near general boundaries. These conditions tend to yield accurate separation lines and separation slopes for steady flows with linear skin-friction fields (cf. §12 and Appendix E) and hence are effective close to skin-friction zeros. Wu *et al.* (2000) demonstrate their result on a flow past a prolate spheroid (see also Wu, Ma & Zhou 2005).

1.2. *Main results*

In the present paper, we develop an exact nonlinear theory of steady flow separation and reattachment on boundaries at rest. We obtain criteria phrased in Eulerian (lab-frame-based) quantities, but our techniques stem from the Lagrangian ideas of Shen (1978), Van Dommelen & Shen (1980), Wu *et al.* (1987) and Van Dommelen & Cowley (1990). Arguably, it is Lagrangian separation that is observed in most flow-visualization experiments, including particle image velocimetry (PIV) and smoke or dye experiments with weakly diffusive substances.

We link separation to the existence of unstable manifolds emanating from the no-slip boundary. These manifolds are material curves or surfaces that collect and eject fluid particles from the vicinity of the boundary. One-dimensional unstable manifolds (separation profiles) emanate from zeros of the skin-friction field; such manifolds can be found and approximated by classic results in nonlinear dynamics. By contrast, two-dimensional unstable manifolds (separation surfaces) emanate from distinguished skin-friction lines, the separation lines. Most of our effort goes into identifying such lines.

We argue that the distinguishing feature of separation lines is their strong saddle-type instability relative to an appropriately rescaled local flow near the boundary. We

identify such instabilities by solving the time-dependent equation of variations along scaled skin-friction lines.

As a result, we obtain asymptotic conditions for separation lines and explicit formulae for separation angles. Invoking the Poincaré–Bendixson theory of planar vector fields and using invariant manifold theory, we find that only four types of locally unique separation lines are possible in physical fluid flows: (S1) saddle–spiral connections; (S2) saddle–node connections; (S3) saddle–limit cycle connections and (S4) limit cycles.

(S1) and (S2) separation have been known as closed separation; (S3) and (S4) separation are undocumented, even though (S3)-type skin-friction patterns have been observed in at least one instance (Hsieh & Wang 1996). Based on common terminology, the latter two separation types should be characterized as open. They differ from common examples of open separation in that they admit unique separation lines and surfaces (cf. §11).

For all four types of separation, we give conditions under which regular (i.e. unique, bounded, smooth, and robust) separation surfaces emerge from the wall. We also obtain first-order approximations for these surfaces from our separation angle formula.

We test our theory on analytic flow models derived from the Taylor expansion of the Navier–Stokes equations at a boundary point (Perry & Chong 1986). These flow models are sophisticated enough to exhibit the four basic separation types, yet do not pose computational or experimental difficulties that would obstruct the accuracy of our predictions. A verification of our results in direct numerical simulations appears in Surana, Jacobs & Haller (2005).

2. Set-up and assumptions

Consider a three-dimensional steady velocity field

$$v(x, y, z) = (u(x, y, z), v(x, y, z), w(x, y, z)). \tag{2.1}$$

For simplicity, assume that the flow generated by v admits a flat boundary satisfying $z = 0$; §9 will describe the treatment of general boundaries.

On the $z = 0$ boundary, v satisfies the no-slip boundary condition

$$u(x, y, 0) = v(x, y, 0) = w(x, y, 0) = 0. \tag{2.2}$$

In our notation, we distinguish the velocity components parallel to the boundary by letting

$$x = (x, y), \qquad u(x, z) = (u(x, y, z), v(x, y, z)), \qquad w(x, z) = w(x, y, z).$$

We assume that the fluid satisfies the steady continuity equation

$$\nabla \cdot (\rho v) = 0, \tag{2.3}$$

where ρ denotes the density of the fluid. Then (2.2) and (2.3) imply that the flow is incompressible along the boundary:

$$\nabla \cdot v(x, 0) = 0. \tag{2.4}$$

Using the no-slip boundary conditions (2.2) and the local incompressibility condition (2.4), we rewrite the velocity field as

$$u(x, z) = z A(x, z), \qquad w(x, z) = z^2 C(x, z), \tag{2.5}$$

where

$$A(x, z) = \int_0^1 \partial_z u(x, qz) \, dq, \qquad C(x, z) = \int_0^1 \int_0^1 \partial_z^2 w(x, qrz)r \, dr \, dq. \qquad (2.6)$$

With this notation, (2.3) becomes

$$\nabla \rho \cdot (zA, \, z^2 C) + \rho z \left[\nabla_x \cdot A + 2C + z \partial_z C \right] = 0,$$

where $\nabla_x = e_x \partial_x + e_y \partial_y$, and e_x and e_y are unit vectors along the x- and y-axes. The above must hold for all z; therefore, we must have

$$\nabla \rho \cdot (A, \, zC) + \rho \left[\nabla_x \cdot A + 2C + z \partial_z C \right] = 0. \qquad (2.7)$$

By (2.5), fluid particle motions satisfy the differential equations

$$\dot{x} = zA(x, z), \qquad \dot{z} = z^2 C(x, z), \qquad (2.8)$$

for which the $z = 0$ plane is a set of fixed points, a highly degenerate object. We remove this degeneracy by introducing the rescaled time

$$s = \int_{t_0}^t z(r) \, dr \qquad (2.9)$$

along each trajectory $(x(t), z(t))$ of (2.8) (see, e.g. Wu *et al.* 1987). With the scaling (2.9) equation (2.8) becomes

$$x' = A(x, z), \qquad z' = zC(x, z), \qquad (2.10)$$

with the prime referring to differentiation with respect to s. As (2.7) shows, the rescaled flow (2.10) is compressible at the wall except at points where $C(x, 0) = 0$. Note that s is a well-defined time-like variable for (2.10) even on the boundary, although the transformation (2.9) between (2.8) and (2.10) breaks down at $z = 0$.

The trajectories of the scaled flow (2.10) are identical to those of (2.8) away from the boundary. On the boundary, however, (2.10) generates fictitious trajectories tangent to the skin-friction field

$$\tau(x) = \rho \nu A(x, 0) = \rho \nu \partial_z u(x, 0), \qquad (2.11)$$

with ν denoting the kinematic viscosity of the fluid. In general, both ρ and ν are functions of x on the boundary.

Another quantity of interest will be the wall-vorticity field

$$\omega(x) = A^\perp(x, 0) = \partial_z u^\perp(x, 0), \qquad (2.12)$$

where we used the notation $(a, b)^\perp = (-b, a)$.

3. Separation and reattachment definitions

We say that the flow separates at the $z = 0$ boundary if fluid particles near the boundary converge to a streamline $\mathscr{L}$ (*separation profile*) or a streamsurface $\mathscr{S}$ (*separation surface*), along which they are ejected from the boundary. In the language of nonlinear dynamics, $\mathscr{L}$ is a one-dimensional unstable manifold of a boundary point (*separation point*); $\mathscr{S}$ is a two-dimensional unstable manifold of a curve of boundary points (*separation line*), as shown in figure 1.

Unstable manifolds are invariant: particles starting on them remain on them for all times. Unstable manifolds are, therefore, material lines or surfaces that remain
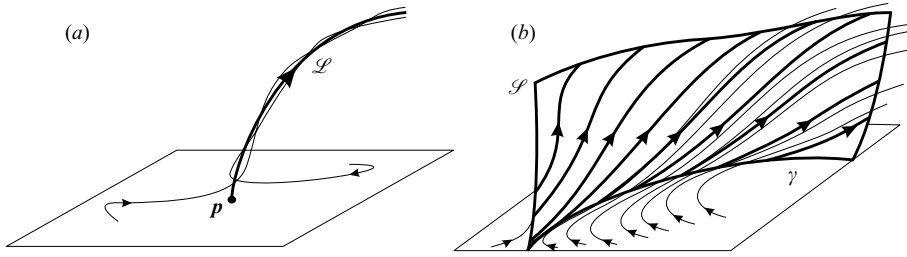
FIGURE 1. (*a*) Separation profile $\mathscr{L}$ emanating from a separation point $\boldsymbol{p}$. (*b*) Separation surface $\mathscr{S}$ emanating from a separation line γ.
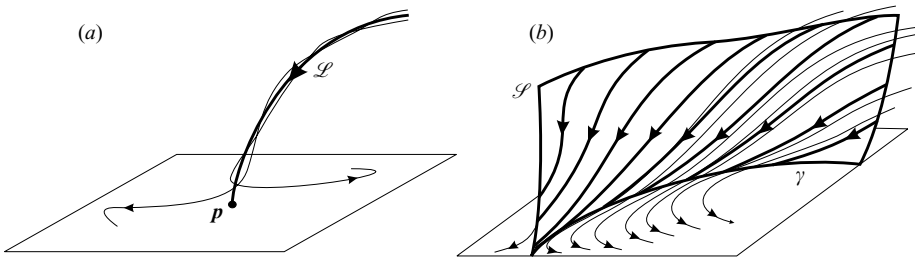
FIGURE 2. (*a*) Reattachment profile $\mathscr{L}$ emanating from a reattachment point $\boldsymbol{p}$. (*b*) Reattachment surface $\mathscr{S}$ emanating from a reattachment line γ.

undeformed by the flow in time. Because we consider steady flows, material lines and material surfaces are streamlines and streamsurfaces, respectively.

To exclude unphysical cases, we shall only consider separation profiles and surfaces that are:

  (i) Unique: no other separation profile or surface emerges from the same set of boundary points. Also, nearby boundary points admit no separation profiles or surfaces.

 (ii) Bounded: they intersect the boundary in a bounded set.

(iii) Smooth: they are continuously differentiable.

(iv) Robust: they smoothly deform but survive under small perturbations to $\boldsymbol{v}$.

Properties (i)–(iii) express plausible physical features of separation; property (iv) excludes degenerate separation patterns that are not reproducible experimentally or numerically. Such patterns, as it turns out, include separation profiles and surfaces tangent to the boundary.

We define reattachment as separation exhibited by the flow in backward time. A *reattachment point* is, therefore, a boundary point with a one-dimensional stable manifold (*reattachment profile*), and a *reattachment line* is a boundary curve with a two-dimensional stable manifold (*reattachment surface*), as shown in figure 2. Again, we require properties (i)–(iv) for reattachment profiles and surfaces. Just like unstable manifolds, stable manifolds are also invariant material surfaces.

4. Separation points and profiles

4.1. *Separation points*

A separation profile $\mathscr{L}$ for the fluid flow (2.8) is also an invariant curve for the scaled flow (2.10), because the trajectories of (2.8) and (2.10) coincide away from the boundary. As a result, the intersection point $\boldsymbol{p}$ of $\mathscr{L}$ with the invariant plane $\{z = 0\}$

must be invariant under the scaled flow. The point $\boldsymbol{p}$ is, therefore, a fixed point of (2.10), i.e. a zero of the skin-friction field (2.11):

$$A(\boldsymbol{p}, 0) = \partial_z \boldsymbol{u}(\boldsymbol{p}, 0) = \boldsymbol{0}. \tag{4.1}$$

The fixed point $\boldsymbol{p}$ admits an unstable manifold satisfying the properties (i)–(iv) if and only if the linearized scaled flow,

$$\begin{pmatrix} \boldsymbol{\xi}' \\ \eta' \end{pmatrix} = \begin{pmatrix} \nabla_x A(\boldsymbol{p}, 0) & \partial_z A(\boldsymbol{p}, 0) \\ \boldsymbol{0} & C(\boldsymbol{p}, 0) \end{pmatrix} \begin{pmatrix} \boldsymbol{\xi} \\ \eta \end{pmatrix}, \tag{4.2}$$

has a single positive eigenvalue with the corresponding eigenvector transverse to the $z = 0$ plane. This follows from the stable manifold theorem for fixed points of vector fields (see Guckenheimer & Holmes 1983).

The eigenvalues λ_i of the linear system (4.2) satisfy

$$\lambda_1 + \lambda_2 = \nabla_x \cdot A(\boldsymbol{p}, 0), \qquad \lambda_3 = C(\boldsymbol{p}, 0). \tag{4.3}$$

Because the eigenvector corresponding to λ_3 is the only one off the boundary, and λ_3 is the only one that is positive, we must have

$$\det \nabla_x A(\boldsymbol{p}, 0) > 0, \qquad \nabla_x \cdot A(\boldsymbol{p}, 0) < 0, \tag{4.4}$$

at the separation point.

In conclusion, (2.11), (4.1) and (4.4) give the following sufficient and necessary conditions for a separation point $\boldsymbol{p}$ to exist on the boundary:

$$\boldsymbol{\tau}(\boldsymbol{p}) = 0, \quad \det \nabla_x [\boldsymbol{\tau}/(\rho\nu)]_{x=p} > 0, \quad \nabla_x \cdot [\boldsymbol{\tau}/(\rho\nu)]_{x=p} < 0, \quad \partial_z^2 w(\boldsymbol{p}, 0) > 0. \tag{4.5}$$

Reattachment points, by contrast, satisfy

$$\boldsymbol{\tau}(\boldsymbol{p}) = 0, \quad \det \nabla_x [\boldsymbol{\tau}/(\rho\nu)]_{x=p} > 0, \quad \nabla_x \cdot [\boldsymbol{\tau}/(\rho\nu)]_{x=p} > 0, \quad \partial_z^2 w(\boldsymbol{p}, 0) < 0. \tag{4.6}$$

4.2. *Separation profiles*

Recall that a separation profile $\mathscr{L}$ is the off-wall streamline emanating from a separation point $\boldsymbol{p}$. Let $\mathscr{L}$ be locally represented by

$$\boldsymbol{x} = \boldsymbol{p} + z\boldsymbol{G}(z), \tag{4.7}$$

where $\boldsymbol{G}$ admits the Taylor-series expansion

$$\boldsymbol{G}(z) = \boldsymbol{g}_0 + z\boldsymbol{g}_1 + \tfrac{1}{2}z^2\boldsymbol{g}_2 + \tfrac{1}{6}z^3\boldsymbol{g}_2 + \cdots \tag{4.8}$$

with

$$\boldsymbol{g}_0 = \boldsymbol{G}(0), \quad \boldsymbol{g}_1 = \partial_z \boldsymbol{G}(0), \quad \boldsymbol{g}_2 = \partial_z^2 \boldsymbol{G}(0), \quad \cdots, \quad \boldsymbol{g}_n = \partial_z^n \boldsymbol{G}(0).$$

Because $\mathscr{L}$ is an invariant curve for the flow (2.8), differentiation of (4.7) in time yields

$$\dot{\boldsymbol{x}} = \dot{z}(\boldsymbol{G}(z) + z\boldsymbol{G}'(z)),$$

or, equivalently,

$$A(\boldsymbol{p} + \boldsymbol{G}(z), z) = zC(\boldsymbol{p} + \boldsymbol{G}(z), z)[\boldsymbol{G}(z) + z\boldsymbol{G}'(z)], \tag{4.9}$$

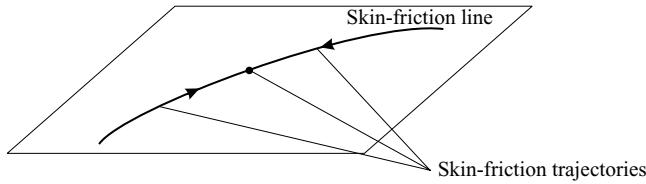as an implicit equation for the separation profile.

FIGURE 3. Skin-friction line consisting of three distinct skin-friction trajectories.

In (4.9), we substitute (4.8) for $\boldsymbol{G}$ and Taylor-expand at $z = 0$. Comparing the $O(z)$ terms on both sides gives an expression for the slope of the separation profile,

$$\boldsymbol{g}_0 = -\left[2\nabla_x[\boldsymbol{\tau}/(\rho\nu)] - \partial_z^2 w(\boldsymbol{p}, 0)\boldsymbol{I}\right]^{-1}\partial_z^2 \boldsymbol{u}(\boldsymbol{p}, 0), \qquad (4.10)$$

with $\boldsymbol{I}$ denoting the two-dimensional identity matrix.

Equating the $O(z^2)$ terms in (4.9) gives an expression for the separation curvature:

$$\begin{aligned}
\boldsymbol{g}_1 = \tfrac{1}{2}\left[\nabla_x \partial_z \boldsymbol{u}(\boldsymbol{p}, 0) - \partial_z^2 w(\boldsymbol{p}, 0)\,\boldsymbol{I}\right]^{-1} \\
\times \Big\{-\tfrac{1}{3}\partial_z^3 \boldsymbol{u}(\boldsymbol{p}, 0) + \left[\tfrac{1}{3}\partial_z^3 w(\boldsymbol{p}, 0)\boldsymbol{I} - 3\nabla_x\partial_z^2 \boldsymbol{u}(\boldsymbol{p}, 0)\right]\boldsymbol{g}_0 \\
+ 2\left[-\nabla_x^2\partial_z^2 \boldsymbol{u}(\boldsymbol{p}, 0)\boldsymbol{g}_0 + \left(\nabla_x\partial_z^2 w(\boldsymbol{p}, 0)\boldsymbol{g}_0\right)\boldsymbol{I}\right]\boldsymbol{g}_0\Big\}.
\end{aligned} \qquad (4.11)$$

The above slope and curvature formulae are equally valid for reattachment profiles. Higher-order approximations for separation and reattachment profiles can be obtained by comparing the higher-order terms in (4.9).

5. Separation lines

5.1. *Skin-friction lines*

A separation surface $\mathscr{S}$ for the fluid flow (2.8) is an invariant surface for the scaled flow (2.10). As a result, a separation line γ, the intersection of $\mathscr{S}$ with the invariant plane $\{z = 0\}$, must be an invariant curve for (2.10). By (2.11), such an invariant curve is a skin-friction line, i.e. a smooth curve tangent to the skin-friction field $\boldsymbol{\tau}(\boldsymbol{x})$.

A skin-friction line, however, is typically not a single trajectory of (2.10); rather, it is a connected union of such trajectories, with each trajectory $\boldsymbol{x}(s; \boldsymbol{x}_0)$ satisfying

$$\boldsymbol{x}'(s; \boldsymbol{x}_0) = \boldsymbol{A}(\boldsymbol{x}(s; \boldsymbol{x}_0), 0), \qquad \boldsymbol{x}(0; \boldsymbol{x}_0) = \boldsymbol{x}_0, \qquad (5.1)$$

as shown in figure 3.

The fundamental question of three-dimensional separation is the following: What distinguishes separation lines from other skin-friction lines? As we argue below, their distinguishing feature is strong hyperbolicity.

5.2. *Strong hyperbolicity*

A skin-friction line γ is *strongly hyperbolic* with respect to the scaled flow (2.10) if: (i) some infinitesimally close trajectories of (2.10) are attracted to γ in forward time and repelled by γ in backward time; (ii) other infinitesimally close trajectories of (2.10) are attracted to γ in backward time and repelled by γ in forward time; (iii) all these attraction and repulsion rates are non-degenerate, i.e. exponential in the rescaled time s.

If the forward-time attracted trajectories lie in the $z = 0$ plane and the backward-time attracted ones lie off the $z = 0$ plane, we call γ *strongly S-hyperbolic* with respect to (2.10), with S referring to separation. If the forward-time attracted trajectories lie off the $z = 0$ plane and the backward-time attracted ones lie in the $z = 0$ plane, we

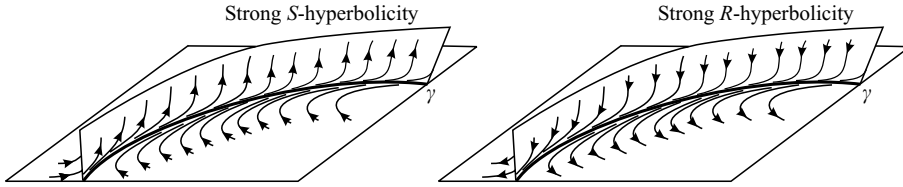Strong *S*-hyperbolicity   Strong *R*-hyperbolicity

FIGURE 4. *S*-type and *R*-type strong hyperbolicity of a skin-friction line with respect to the scaled flow (2.10).
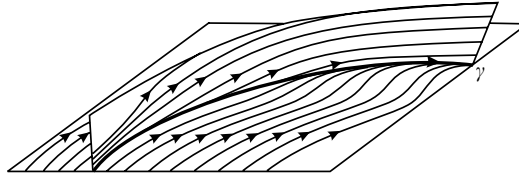

FIGURE 5. Hyperbolic but not strongly hyperbolic skin-friction line in the scaled flow (2.10).

call γ is *strongly R-hyperbolic* with respect to (2.10), with R referring to reattachment (see figure 4).

The qualifier *strong* in the above definitions signals a difference from the classical definition of hyperbolicity in dynamical systems (see, e.g. Fenichel 1971). Specifically, classical definitions only require some trajectories to be exponentially attracted to γ in forward time (but not necessarily repelled by γ in backward time), and other trajectories to be exponentially attracted to γ in backward time (but not necessarily repelled by γ in forward time).

As a result, classical hyperbolicity does not necessarily describe experimentally or numerically observable separation along γ: it only requires γ to collect tracers near the wall for large s values. Tracers, therefore, may only accumulate near a part of γ, as shown in figure 5. The same figure also highlights another shortcoming of classical hyperbolicity in describing observable separation: tracers may not be ejected everywhere along γ.

6. Criteria for separation and reattachment lines

Any bounded skin-friction line γ with strong S-hyperbolicity is a separation-line candidate: tracers along the wall converge towards γ then leave the vicinity of the wall due to the instability of γ. To find actual separation lines, we have to find computable conditions under which: (*a*) a skin-friction line γ is strongly S-hyperbolic; (*b*) a separation surface $\mathscr{S}$ satisfying properties (i)–(iv) of § 3 emerges from the wall along γ.

As we show in Appendix A, a bounded skin-friction line γ is a *separation line* if and only if one of the following holds (see figure 6):

(S1) γ originates from a saddle $\boldsymbol{p}$ with $\partial_z^2 w(\boldsymbol{p}, 0) > 0$, and ends at a stable spiral $\boldsymbol{q}$ with $\partial_z^2 w(\boldsymbol{q}, 0) > 0$.

(S2) γ originates from a saddle $\boldsymbol{p}$ with $\partial_z^2 w(\boldsymbol{p}, 0) > 0$, and ends at a stable node $\boldsymbol{q}$ with $\partial_z^2 w(\boldsymbol{q}, 0) > 0$. Also, γ is tangent to the direction of weaker attraction at $\boldsymbol{q}$.

(S3) γ originates from a saddle $\boldsymbol{p}$ with $\partial_z^2 w(\boldsymbol{p}, 0) > 0$, and spirals onto a stable limit cycle Γ with $\int_\Gamma \partial_z^2 w(\boldsymbol{x}(s; \boldsymbol{x}_0), 0) \, ds > 0$.

(S4) γ is a stable limit cycle with $\int_\gamma \partial_z^2 w(\boldsymbol{x}(s; \boldsymbol{x}_0), 0) \, ds > 0$.
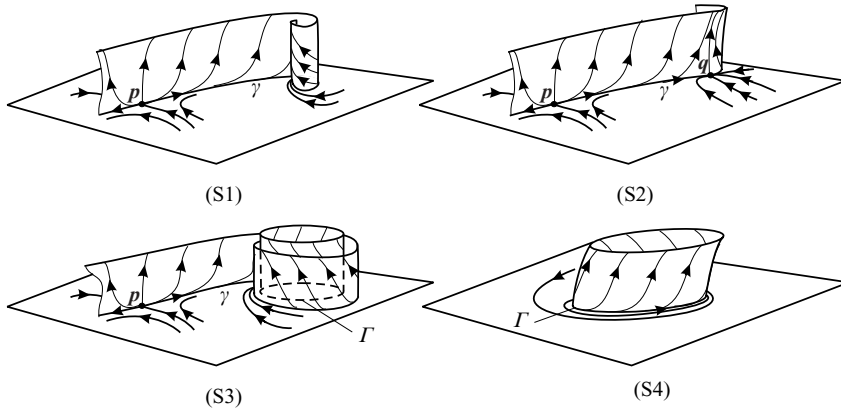
FIGURE 6. The four basic separation patterns satisfying properties (i)–(iv) of §3. For an open–closed classification of these patterns, see §11.
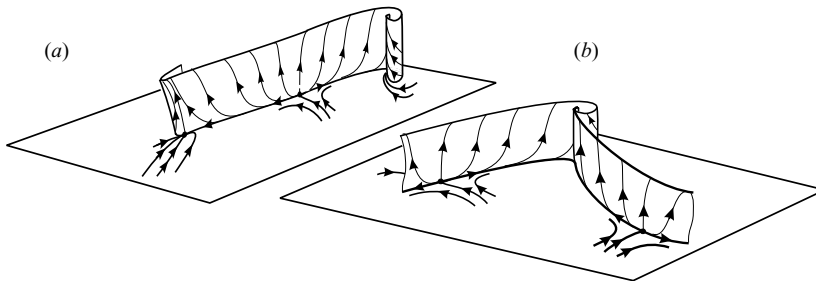

FIGURE 7. (*a*) (S1) and (S2) separation lines emanating from the same saddle-type skin-friction zero. (*b*) Two (S2) separation lines terminating at the same spiral-type skin-friction zero.

All skin-friction zeros and limit cycles featured in (S1)–(S4) must be non-degenerate, i.e. must attract or repel nearby skin-friction trajectories exponentially in the rescaled time s. This will generically be the case away from corners formed by the $z = 0$ plane and another no-slip wall. For completeness, however, we compute all non-degeneracy conditions in Appendix B, and discuss separation near corners in §8.

Since the unstable manifold of a saddle-type skin-friction zero always has two components, a combination of the (S1) and (S2) separation may also arise, as shown in figure 7(*a*). Two identical separation types may also coexist and terminate at the same skin-friction zero or limit cycle, as shown in figure 7(*b*).

The above separation criterion extends to curved boundaries and spheroid surfaces, as discussed in §9. For incompressible Navier–Stokes flows, the criterion can be reformulated using wall pressure and skin friction only (see §10). We discuss the practical implementation of the criterion in §12.1.

Similar results apply to reattachment lines after a reversal of time: a bounded skin-friction line γ on the $z = 0$ boundary is a *reattachment line* if and only if one of the following holds:

(R1) γ originates from an unstable spiral $\boldsymbol{p}$ where $\partial_z^2 w(\boldsymbol{p}, 0) < 0$, and ends at a saddle $\boldsymbol{q}$ where $\partial_z^2 w(\boldsymbol{q}, 0) < 0$.

(R2) γ originates from an unstable node $\boldsymbol{p}$ with $\partial_z^2 w(\boldsymbol{p}, 0) < 0$, and ends at a saddle $\boldsymbol{q}$ with $\partial_z^2 w(\boldsymbol{q}, 0) < 0$. Also, γ is tangent to the direction of weaker repulsion at $\boldsymbol{p}$.
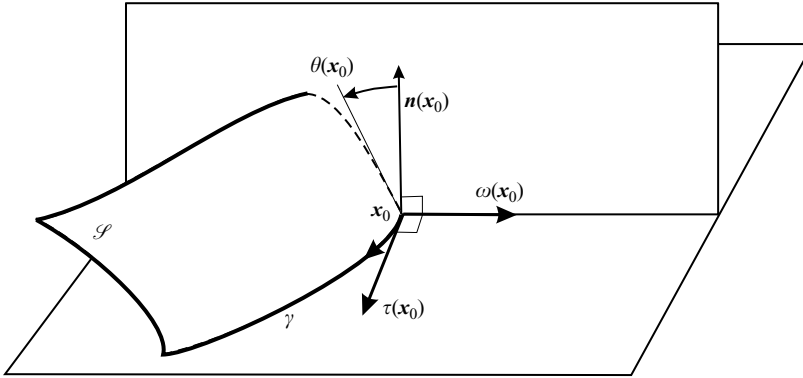
FIGURE 8. Definition of the separation angle.

(R3) γ spirals off from an unstable limit cycle Γ with $\int_{\Gamma} \partial_z^2 w(\boldsymbol{x}(s;\boldsymbol{x}_0),0)\,\mathrm{d}s < 0$, and ends at a saddle $\boldsymbol{q}$ with $\partial_z^2 w(\boldsymbol{q},0) < 0$.

(R4) γ is an unstable limit cycle with $\int_{\gamma} \partial_z^2 w(\boldsymbol{x}(s;\boldsymbol{x}_0),0)\,\mathrm{d}s < 0$.

We list the corresponding non-degeneracy conditions in Appendix B. Reattachment near transverse no-slip walls, on curved boundaries, and on spheroid surfaces can again be analysed based on §§ 8 and 9 below. As in the case of separation, the conditions (R1)–(R4) can be verified from wall-pressure and skin-friction measurements in incompressible Navier–Stokes flows (see § 10).

7. Slope of separation and reattachment surfaces

We define the separation angle $\theta(\boldsymbol{x}_0)$ at a point $\boldsymbol{x}_0$ of a separation line γ as the angle between the wall normal and the tangent of the curve that lies in the intersection of $\mathscr{S}$ with a plane normal to γ (see figure 8).

As shown in Appendix A, the separation slope satisfies

$$\tan\theta(\boldsymbol{x}_0) = \int_{-\infty}^{0} \exp\left(\int_0^s [C(\boldsymbol{x}(r;\boldsymbol{x}_0),0) - S_\perp(r)]\,\mathrm{d}r\right) \frac{\partial_z^2 \boldsymbol{u}\cdot\boldsymbol{\omega}}{2|\boldsymbol{\omega}|}\bigg|_{\boldsymbol{x}=\boldsymbol{x}(s,\boldsymbol{x}_0),z=0}\,\mathrm{d}s, \quad (7.1)$$

where

$$S_\perp(s) = \frac{\boldsymbol{\omega}\cdot(\nabla_{\boldsymbol{x}}[\boldsymbol{\tau}/(\rho\nu)]\,\boldsymbol{\omega})}{|\boldsymbol{\omega}|^2}\bigg|_{\boldsymbol{x}=\boldsymbol{x}(s,\boldsymbol{x}_0)} \quad (7.2)$$

measures the skin-friction stretching rate normal to the skin-friction trajectory $\boldsymbol{x}(s,\boldsymbol{x}_0)$ starting from $\boldsymbol{x}_0$ at time $s=0$.

Reattachment slopes obey a similar formula with the limit taken in forward time:

$$\tan\theta(\boldsymbol{x}_0) = -\int_0^{+\infty} \exp\left(\int_0^s [C(\boldsymbol{x}(r;\boldsymbol{x}_0),0) - S_\perp(r)]\,\mathrm{d}r\right) \frac{\partial_z^2 \boldsymbol{u}\cdot\boldsymbol{\omega}}{2|\boldsymbol{\omega}|}\bigg|_{\boldsymbol{x}=\boldsymbol{x}(s,\boldsymbol{x}_0),z=0}\,\mathrm{d}s. \quad (7.3)$$

8. Separation at corners

Consider a backward-facing step shown in figure 9. Here skin-friction trajectories in the $z=0$ plane approach lines of skin-friction zeros at corner of the $x=0$ and $y=0$ walls.

Let γ be the skin-friction line intersecting the $x=0$ vertical wall at the saddle point $\boldsymbol{p}$. Then γ, a reattachment line candidate, is not strongly R-hyperbolic, because it
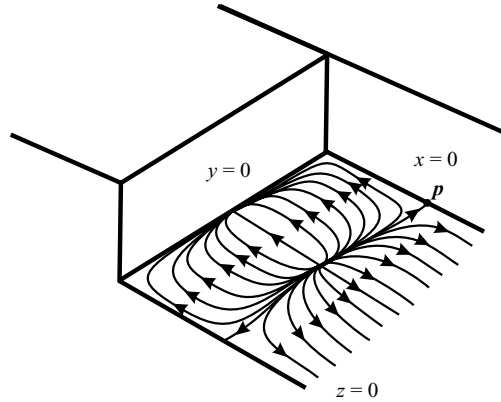
FIGURE 9. Skin-friction trajectories behind a backward-facing step.

does not repel other skin-friction trajectories at an exponential rate in the rescaled time s. Rather, γ repels trajectories at an algebraic rate due to the line of degenerate skin-friction zeros through $\boldsymbol{p}$.

Observe, however, that the analogue of the no-slip boundary conditions (2.2) now also holds at the $x = 0$ wall, allowing us to recast the particle ODE (2.8) in the form

$$\dot{x} = x^2 z \bar{A}(\boldsymbol{x}, z), \quad \dot{y} = xz\bar{B}(\boldsymbol{x}, z), \quad \dot{z} = xz^2 \bar{C}(\boldsymbol{x}, z), \tag{8.1}$$

with

$$\bar{A}(\boldsymbol{x}, z) = \int_0^1 \int_0^1 \int_0^1 \partial_{xxz}^3 u(rqx, y, sz) q \, \mathrm{d}q \, \mathrm{d}s \, \mathrm{d}r,$$

$$\bar{B}(\boldsymbol{x}, z) = \int_0^1 \int_0^1 \partial_{xz}^2 v(rx, y, sz) \, \mathrm{d}s \, \mathrm{d}r,$$

$$\bar{C}(\boldsymbol{x}, z) = \int_0^1 \int_0^1 \int_0^1 \partial_{xzz}^3 w(rx, y, sqz) q \, \mathrm{d}q \, \mathrm{d}s \, \mathrm{d}r.$$

Now, instead of (2.9), we introduce the new time

$$s = \int_{t_0}^t x(r) z(r) \, \mathrm{d}r \tag{8.2}$$

along each trajectory of (8.1) to obtain the rescaled equations of particle motion

$$\boldsymbol{x}' = \bar{\boldsymbol{A}}(\boldsymbol{x}, z), \qquad z' = z\bar{C}(\boldsymbol{x}, z), \tag{8.3}$$

with

$$\bar{\boldsymbol{A}} = (x\bar{A}, \bar{B}),$$

and with the prime referring to differentiation with respect to s as defined in (8.2). In the rescaled system (8.3), γ is strongly hyperbolic if no higher-order degeneracies are present at the corner.

By analogy between (2.10) and (8.3), all our separation results carry over to the present case if we replace (A, C) with $(\bar{A}, \bar{C})$. Specifically, the non-degeneracy conditions of Appendix B and the slope formula (7.1) should be evaluated using $\bar{A}$ and $\bar{C}$. Curved vertical walls can be treated by combining the present approach with that of § 9 below.

9. Separation on curved boundaries and spheroids

9.1. *Curved boundaries*

Keeping the notation $x = (x, y)$, we now assume that the flow boundary satisfies $z = f(x)$ for some smooth function $f(x)$. The no-slip boundary condition for the velocity field $v = (u, v, w)$ then becomes

$$u(x, f(x)) = v(x, f(x)) = w(x, f(x)) = 0.$$

As earlier, we assume that the steady continuity equation (2.3) holds, which again implies local incompressibility along the boundary:

$$\nabla \cdot v(x, f(x)) = 0. \tag{9.1}$$

We flatten out the boundary by replacing z with the new coordinate

$$\tilde{z} = z - f(x),$$

which transforms the particle motion equations (2.8) to the form

$$\frac{\mathrm{d}}{\mathrm{d}t} x = \tilde{u}(x, \tilde{z}), \qquad \frac{\mathrm{d}}{\mathrm{d}t} \tilde{z} = \tilde{w}(x, \tilde{z}), \tag{9.2}$$

with

$$\tilde{u}(x, \tilde{z}) = u(x, \tilde{z} + f(x)), \qquad \tilde{w}(x, \tilde{z}) = w(x, \tilde{z} + f(x)) - \nabla_x f(x) \cdot u(x, \tilde{z} + f(x)).$$

Because

$$\det \left[\frac{\partial(x, \tilde{z})}{\partial(x, z)} \right] = 1,$$

the transformation $(x, z) \mapsto (x, \tilde{z})$ preserves volume. As a result, the flow remains locally incompressible in the $(x, \tilde{z})$ coordinates along the $\tilde{z} = 0$ boundary. The transformed velocity field $\tilde{v} = (\tilde{u}, \tilde{w})$, therefore, can again be written in the form

$$\tilde{u}(x, \tilde{z}) = \tilde{z} \tilde{A}(x, \tilde{z}), \qquad \tilde{w}(x, \tilde{z}) = \tilde{z}^2 \tilde{C}(x, \tilde{z}), \tag{9.3}$$

with the functions

$$\tilde{A}(x, \tilde{z}) = \int_0^1 \partial_{\tilde{z}} \tilde{u}(x, s\tilde{z}) \, \mathrm{d}s, \qquad \tilde{C}(x, \tilde{z}) = \int_0^1 \int_0^1 \partial_{\tilde{z}}^2 \tilde{w}(x, sq\tilde{z}) q \, \mathrm{d}q \, \mathrm{d}s.$$

By analogy between (2.5) and (9.3), our previous results for separation on flat boundaries carry over to the present case. Specifically, if instead of the true skin-friction and wall-vorticity fields, we use their x-projections,

$$\left. \begin{aligned} \tau(x) &= \rho \nu \partial_z u(x, f(x)), \\ \omega(x) &= A^\perp(x, f(x)), \end{aligned} \right\} \tag{9.4}$$

then the separation and reattachment criteria of §6 continue to hold.

The separation slope and curvature formulae also remain valid in the $(\tilde{x}, z)$ coordinates, as long as we evaluate (4.10), (4.11) and (7.1) at $z = f(x)$ instead of $z = 0$. In Appendix C, we derive an expression for the separation slope in the original (x, z) coordinates.

9.2. *Spheroids*

Spheroids are surfaces obtained from smooth deformations of a two-dimensional sphere (see figure 10). Such surfaces can always be written locally as a smooth graph
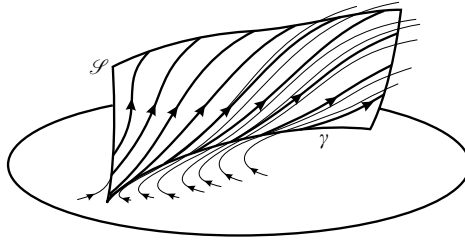
FIGURE 10. Separation on a spheroid surface.

$z = f(x)$, and hence separation and reattachment on them can locally be studied using the approach of §9.1 above.

Our mathematical argument in Appendix A, however, also utilizes the global geometry of the boundary. Specifically, a crucial ingredient, the classic Poincaré–Bendixson theory (see, e.g. Guckenheimer & Holmes 1983), applies to bounded planar skin-friction fields. By this theory, all bounded skin-friction lines must emanate from, and converge to, one of the following types of sets: a skin-friction zero, a skin-friction limit cycle, or a set of skin-friction zeros connected by skin-friction trajectories.

The classic Poincaré–Bendixson theory, however, extends to any surface that is diffeomorphic to a sphere, i.e. any surface that is the image of a sphere under a continuously differentiable invertible mapping with a differentiable inverse (see Hartman 1982). As a result, the separation theory developed here carries over to common aerodynamic objects, such as ordinary airfoils, fuselages, projectiles, and prolate spheroids.

Boundaries that are formally not covered by our theory are two-dimensional manifolds on which the Poincaré–Bendixson theory fails: toroidal surfaces and surfaces with handles. Our results, however, do apply even to such boundaries if the separation or reattachment line γ is fully contained in a boundary domain satisfying $z = f(x)$ (cf. (9.1)).

10. Separation in incompressible Navier–Stokes flows

For incompressible flows, the steady continuity equation (2.3) and $\nabla \cdot \boldsymbol{v} = 0$ yield

$$\boldsymbol{v} \cdot \nabla \rho = z\, [\nabla \rho \cdot (\boldsymbol{A}, zC)] = 0.$$

This equation must hold for all z, thus $\nabla \rho \cdot (\boldsymbol{A}, zC)$ must vanish for all $z \neq 0$. Then, by continuity, $\nabla \rho \cdot (\boldsymbol{A}, zC)$ must also vanish at $z = 0$, implying

$$\nabla \rho \cdot (\boldsymbol{A}, zC) = 0 \tag{10.1}$$

for all z.

Setting $z = 0$ in (2.7) and using (10.1) then gives

$$\nabla_x \cdot \boldsymbol{A}(\boldsymbol{x}, 0) + 2C(\boldsymbol{x}, 0) = 0. \tag{10.2}$$

We recall the notation introduced in (2.6) and (7.2), and let

$$S_{\parallel}(s) = \left. \frac{\boldsymbol{\tau} \cdot (\nabla_x [\boldsymbol{\tau}/(\rho\nu)]\,\boldsymbol{\tau})}{|\boldsymbol{\tau}|^2} \right|_{\boldsymbol{x} = \boldsymbol{x}(s, \boldsymbol{x}_0)} \tag{10.3}$$

denote the skin-friction stretching rate along $\boldsymbol{x}(s, \boldsymbol{x}_0)$. We can then rewrite (10.2) as

$$\partial_z^2 w(\boldsymbol{x}(s; \boldsymbol{x}_0), 0) = 2C(\boldsymbol{x}(s; \boldsymbol{x}_0), 0) = -\nabla_x \cdot [\boldsymbol{\tau}/(\rho\nu)] = -[S_{\parallel}(s) + S_{\perp}(s)]. \tag{10.4}$$

By (10.4), in the separation criteria of §§4 and 6, the wall-normal derivative

$$\partial_z^2 w = -\nabla_x \cdot [\tau / (\rho\nu)] \tag{10.5}$$

can be computed from on-wall derivatives of the skin-friction field. In addition, by (10.4), the separation slope formula (7.1) takes the form

$$\tan\theta(x_0) = \int_{-\infty}^{0} \exp\left(-\frac{1}{2}\int_{0}^{s}[3S_\perp(r) + S_{\|}(r)]\,dr\right) \frac{\partial_z^2 u \cdot \omega}{2|\omega|}\bigg|_{x=x(s,x_0),z=0} ds. \tag{10.6}$$

For a steady incompressible Navier–Stokes flow with pressure field $p(x, 0)$, the continuity equation (2.3) and the Navier–Stokes equations give

$$\nabla_x \rho(x, 0) = 0, \qquad \partial_z^2 u(x, 0) = \frac{1}{\nu\rho}\nabla_x p(x, 0). \tag{10.7}$$

Then, assuming that $\rho\nu = $ const. along the boundary, we obtain from (10.7), (4.10) and (10.6) the separation slope formulae

$$g_0 = -[2\nabla_x \tau(p) + \nabla_x \cdot \tau(p)I]^{-1}\nabla_x p(x, 0), \tag{10.8a}$$

$$\tan\theta(x_0) = \frac{1}{2\nu\rho}\int_{-\infty}^{0}\exp\left(-\frac{1}{2}\int_{0}^{s}[3S_\perp(r) + S_{\|}(r)]\,dr\right)\frac{\nabla_x p(x, 0)\cdot\omega}{|\omega|}\bigg|_{x=x(s,x_0)} ds. \tag{10.8b}$$

Thus, for incompressible Navier–Stokes flows, the separation slope can also be computed from wall pressure and skin friction. Analogous results hold for reattachment.

Using the slope formulae in (10.8), we can show that *tangential separation* – although theoretically possible – is non-robust and hence is unobservable in incompressible Navier–Stokes flows (cf. Appendix A, § A.7).

11. Open–closed classification of separation patterns

A consequence of the previous sections is the following general result: three-dimensional steady separation or reattachment is either *closed* (γ connects zeros of τ), *open* (γ is a limit cycle of τ), or *open–closed* (γ connects a saddle-type zero of τ to a limit cycle). There is no other steady separation or reattachment pattern that satisfies all the basic requirements (i)–(iv) we put forward in §3.

11.1. *Prior work on open separation*

As noted in the Introduction, open separation (i.e. separation without skin-friction zeros at either end of the separation line) was first observed by Wang (1972). The best known example of open separation (also known as crossflow separation) is that on a round-nosed body of revolution (Wang 1972, 1974, 1983; Tobak & Peake 1982). We sketch the corresponding skin-friction pattern in figure 11.

In an incompressible flow, converging skin-friction lines, such as those in figure 11, indeed lead to the ejection of particles from the vicinity of the boundary. Based on the skin-friction topology, one is tempted to designate the attracting portion of a skin-friction line, such as the dashed segment in figure 11, as a line of separation.

Note, however, that the above designation is arbitrary: the dashed line segment is no more distinguished than any other nearby segment with $S_\perp < 0$: all such segments attract skin-friction lines, connect the same skin-friction zeros, and repel off-wall fluid trajectories owing to $\partial_z^2 w(x, 0) > 0$, which holds by (10.5).
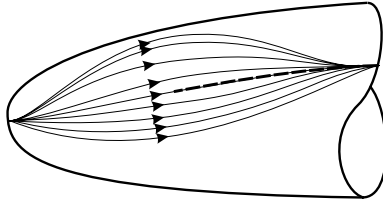
FIGURE 11. Sketch of skin-friction lines on a round-nosed body of revolution at higher angles of attack.
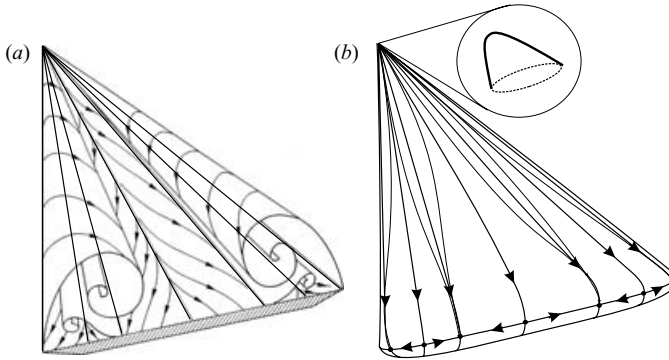

FIGURE 12. (*a*) Common illustration of separation on a delta wing (from Délery 2001). (*b*) Simplest complete separation pattern on the full delta wing.

The skin-friction pattern shown in figure 11, therefore, does not admit a unique separation line or separation surface, thereby violating our basic requirement (i) for separation in §3. Even if one heuristically designates a segment $\tilde{\gamma}$ of a skin-friction line as a separation line, there is no unique separation surface emanating from $\tilde{\gamma}$. Indeed, repeating the derivation of the separation slope formula in Appendix A, §A,4, we find that any material surface emanating from $\tilde{\gamma}$ remains transverse to the boundary while attracting and ejecting nearby fluid particles.

The lack of a unique separation line and surface in crossflow separation has also been noted by Han & Patel (1979), Yates & Chapman (1992) and Wetzel, Simpson & Chesnakas (1998). As a well-defined separation structure in such problems, one may instead choose the one-dimensional separation profile emanating from the attracting skin-friction zero (see figure 19(*c*) for an example).

Another frequently cited example of open separation is that over a delta wing, as sketched in figure 12(*a*). In this example, as often remarked, the straight skin-friction lines emanating from the tip of the wing do not terminate in skin-friction zeros.

Note, however, that the skin-friction pattern in figure 12(*a*) is incomplete. The full wing is a two-dimensional spheroid, thus by the Poincaré–Bendixson theory, all skin-friction lines must emanate from, and converge to, one of the three types of sets described in §9.2: a skin-friction zero, a skin-friction limit cycle, or a set of skin-friction zeros connected by skin-friction trajectories.

A full skin-friction pattern consistent with the Poincaré–Bendixson theory is shown in 12(*b*). This pattern exhibits closed separation: all separation lines connect zeros of the τ-field. The skin-friction lines near the tip may be intricate, but must terminate in one of the three types of sets mentioned above.

Other proposed examples of open separation involve flows defined on infinite domains (Kenwright, Henze & Levit 1999). The Poincaré–Bendixson theory is invalid on unbounded domains: an unbounded separation line may indeed not converge to zeros or limit cycles of the τ-field. In this paper, however, we have excluded unbounded separation lines as unphysical (see (iii) of §3).

In summary, the separation theory described here allows for open separation, but not of the type suggested in earlier studies. Some of those studies proposed examples with incomplete separation patterns; others proposed examples with unbounded or non-unique separation surfaces.

11.2. *Prior work on open-closed separation*

The (S3) open–closed separation described in this paper has apparently been overlooked as a possibility in earlier studies. Hsieh & Wang (1996), however, do observe connections between saddle-type zeros and limit cycles of the skin-friction field on a cylinder with a hemispherical cap.

12. Examples

Here we analyse three-dimensional separation in analytic flow models obtained as truncated expansions of the Navier–Stokes equations near a boundary point (see Perry & Chong 1986). All our models are incompressible and dynamically consistent up to quartic order in the distance from the point of expansion. We give a brief summary of the derivation of these models in Appendix D.

Varying free parameters in our models, we provide examples of the four basic separation patterns (S1)–(S4). We then generate streamlines numerically to confirm the predicted location and slope of the separation surface.

12.1. *Steps in the analysis*

We analyse our flow models through the following steps:

(i) For a given skin-friction field, find all saddles, nodes, foci, and limit cycles.

(ii) For each non-degenerate skin-friction saddle p, find its stable and unstable manifolds in the $z = 0$ plane. $W^u(p)$ is obtained numerically by advecting a small line segment under the scaled flow (2.10); the line segment is initially tangent to the unstable eigenvector of p. $W^s(p)$ is obtained by backward-advecting a small line segment under the scaled flow (2.10); the line segment is initially tangent to the stable eigenvector of p.

(iii) Identify separation and reattachment points using (4.5) and (4.6).

(iv) Identify separation and reattachment lines from the list (S1)–(S4) and (R1)–(R4). Verify non-degeneracy of separation patterns using Appendix B.

(v) Compute the slope of separation and reattachment profiles using (4.10).

(vi) Compute first-order approximations for reattachment and separation surfaces from the slope formula (7.1).

More generally, the above procedure applies to any numerical or experimental flow data on a boundary domain away from vertical walls. Near vertical walls, the procedure changes according to §8 (see Surana, Jacobs & Haller 2005 for examples).

12.2. *Comparison with vorticity-based separation theory*

For all examples below, we also evaluate the vorticity-based separation theory of Wu *et al.* (2000), the only general criterion available for three-dimensional separation. Appendix E contains a summary of this criterion and the corresponding separation-slope formula.
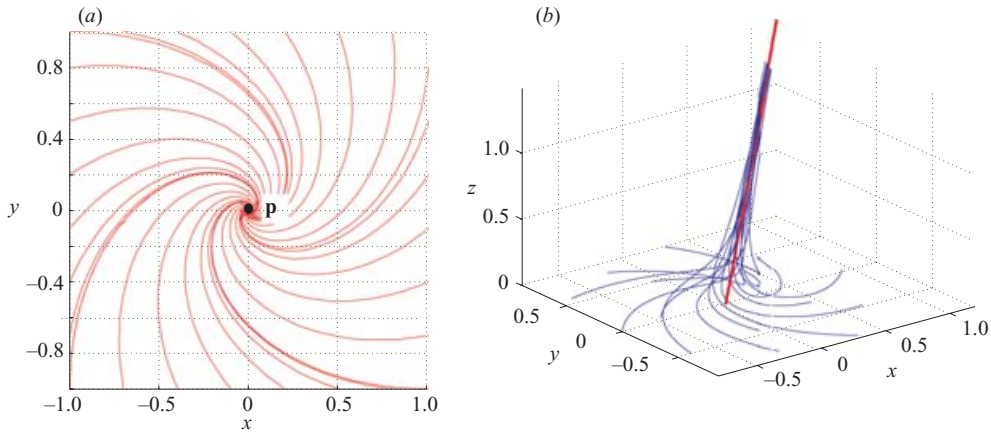
FIGURE 13. (*a*) Skin-friction trajectories for Example I ($\alpha = 1$, $\beta = 2$ and $\delta = 0$). (*b*) Predicted second-order separation profile, and nearby streamlines.

As we shall see, the vorticity-based theory yields inaccurate separation surfaces that intersect – rather than attract and eject – nearby streamlines at the wall. This is because the theory postulates separation lines to be local maximizers (ridges) of the scalar field

$$\varphi(\boldsymbol{x}) = S_\perp(\boldsymbol{x})[S_\perp(\boldsymbol{x}) + S_\parallel(\boldsymbol{x})]/\,|\boldsymbol{\omega}(\boldsymbol{x})|^2\,,$$

even though such ridges only coincide with skin-friction lines if the $\boldsymbol{\tau}$-field is linear (see Appendix E). Near skin-friction zeros, however, the $\boldsymbol{\tau}$-field is close to linear, and hence the vorticity-based prediction for separation lines becomes reasonably accurate.

In the examples admitting separation lines, we shall plot the contours of $\varphi(\boldsymbol{x})$ over domains where the two additional separation conditions of Wu *et al.* (2000), $S_\perp < 0$ and $S_\perp + S_\parallel < 0$, are also satisfied. We shall then locate ridges of $\varphi(\boldsymbol{x})$ for comparison with the exact theory.

12.3. *Example I: Tornado-type separation*

A special case of the model velocity field (D 4) is given by

$$\left.\begin{aligned} u &= -xz + yz + (\alpha + \delta x)z^2, \\ v &= -xz - yz + (\beta + \delta y)z^2, \\ w &= z^2 - (2\delta/3)z^3, \end{aligned}\right\} \tag{12.1}$$

with the skin-friction field:

$$\boldsymbol{\tau} = \begin{pmatrix} -x + y \\ -x - y \end{pmatrix}.$$

This skin-friction field is linear and hence does not admit any limit cycles. The only skin-friction zero is $\boldsymbol{p} = (0, 0)$, for which

$$\det \nabla_{\boldsymbol{x}} \boldsymbol{\tau}(\boldsymbol{p}) = 2 > 0, \qquad \nabla_{\boldsymbol{x}} \cdot \boldsymbol{\tau}(\boldsymbol{p}) = -2 < 0, \qquad \partial_z^2 w(\boldsymbol{p}, 0) = 2 > 0.$$

Thus, by (4.5), $\boldsymbol{p}$ is a separation point with a one-dimensional separation profile that collects and ejects nearby fluid particles. A linear stability analysis reveals that $\boldsymbol{p}$ is an unstable spiral of the skin-friction field (see figure 13a).

Evaluating the slope and curvature formulae (4.10) and (4.11), we find that the separation profile satisfies

$$\begin{pmatrix} x \\ y \end{pmatrix} = z \begin{pmatrix} 2/5 + z\delta/6 & 1/5 + z\delta/6 \\ -1/5 - z\delta/6 & 2/5 + z\delta/6 \end{pmatrix} \begin{pmatrix} \alpha \\ \beta \end{pmatrix} + O(z^3). \tag{12.2}$$

Figure 13(b) confirms that (12.2) is indeed the correct quadratic approximation for the separation profile.

12.4. *Example II: Nonlinear saddle-type separation*

In Appendix D, we obtain the velocity field

$$\left.\begin{aligned} u &= axz - 3dxz^2, \\ v &= -byz + cx^2z - cz^3/3, \\ w &= (b-a)z^2/2 + dz^3, \end{aligned}\right\} \tag{12.3}$$

by applying the Perry–Chong procedure to the skin-friction field

$$\boldsymbol{\tau} = \begin{pmatrix} ax \\ -by + cx^2 \end{pmatrix}, \qquad a, b > 0.$$

Because $\det \nabla_x \boldsymbol{\tau}(\boldsymbol{p}) = -ab < 0$, the point $\boldsymbol{p} = (0, 0)$ is a non-degenerate saddle. We find the skin-friction trajectories by direct integration:

$$\boldsymbol{x}(s; \boldsymbol{x}_0) = \begin{pmatrix} x_0 \, \mathrm{e}^{as} \\ y_0 \mathrm{e}^{-bs} + \dfrac{x_0^2}{2a+b}(\mathrm{e}^{2as} - \mathrm{e}^{-bs}) \end{pmatrix}.$$

Thus, the stable manifold $W^s(\boldsymbol{p})$ of the skin-friction saddle $\boldsymbol{p}$ is the y-axis; the unstable manifold $W^u(\boldsymbol{p})$ satisfies

$$W^u(\boldsymbol{p}) = \left\{ (x, y) \; : \; y = \frac{x^2}{2a+b} \right\},$$

as shown in figure 14(a).

Because only $W^s(\boldsymbol{p})$ and $W^u(\boldsymbol{p})$ connect to a saddle point and there are no limit cycles in the $\boldsymbol{\tau}$-field, only $W^s(\boldsymbol{p})$ and $W^u(\boldsymbol{p})$ are separation- and reattachment-line candidates. Noting that

$$\partial_z^2 w(\boldsymbol{p}, 0) = b - a, \tag{12.4}$$

we find that for $b > a$, the unstable manifold $W^u(\boldsymbol{p})$ is a separation line of type (S1), (S2), (S3) or (S4) on any bounded domain. The actual type of separation depends on the forward-asymptotics of $W^u(\boldsymbol{p})$, a feature uncaptured by our truncated flow model.

In figure 14(b), we show the difference between $\gamma = W^u(\boldsymbol{p})$, the separation line predicted by our theory, and the separation line obtained from the vorticity-based criterion of Wu *et al.* (2000). The difference is small around $\boldsymbol{p}$, but increases as we move away from $\boldsymbol{p}$.

The incompressible formula (10.6) gives the separation slope along γ:

$$\tan\theta(\boldsymbol{x}_0) = \frac{6x_0^2}{(2a+b)\sqrt{4x_0^2 + (2a+b)^2}}, \qquad \boldsymbol{x}_0 = \left(x_0, \frac{x_0^2}{2a+b} \right). \tag{12.5}$$

We also compute the vorticity-based slope prediction (E 7) numerically along the dashed line of figure 14(b); the results are compared in figure 15.
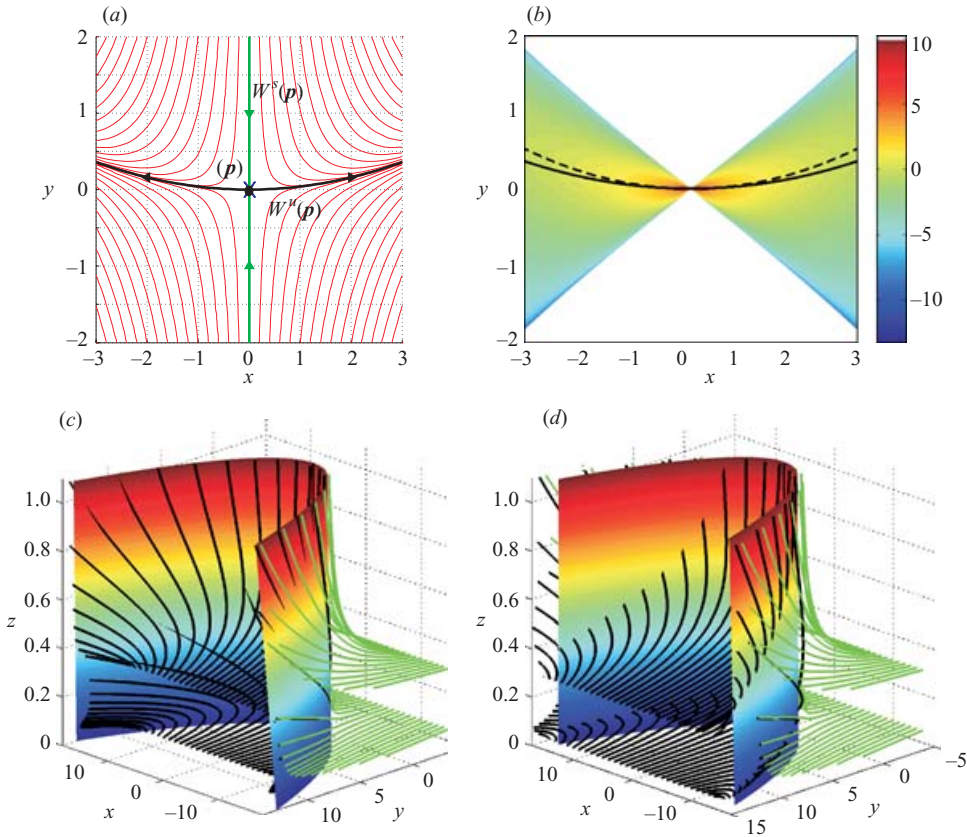
FIGURE 14. Nonlinear saddle-type separation for $a = 1$, $b = 1$, $c = 1$ and $d = 0.5$. (a) Skin-friction trajectories. (b) Exact separation line (solid) and its vorticity-based prediction (dashed), the ridge of the scalar field φ. The contours of φ are shown over the region where (E 4) holds. (c) Linear prediction for the separation surface by our exact theory; also shown are nearby streamlines, started in two different z-planes, in different colours on opposite sides of the surface. (d) As (c) but for the vorticity-based separation theory.

The numerically generated streamlines in figure 14(c) confirm that $\gamma = W^u(\boldsymbol{p})$ is the correct separation line, and (12.5) is the correct separation slope. Indeed, black and green streamlines started on different sides of the predicted separation surface asymptote to the surface. By contrast, figure 14(d) shows the first-order separation surface predicted by the theory of Wu *et al.* (2000). In this case, streamlines released on different sides of the predicted surface intersect the surface even near the wall, hence the vorticity-based prediction is inaccurate.

12.5. *Example III: Separation-bubble flow*

In Appendix D, we derive the separation-bubble flow

$$
\left.
\begin{aligned}
u &= z[(x/a)^2 + (y/b)^2 - 1] + z^2[\alpha + \delta x + (c/6 - 2/(3a^2) - 1/(3b^2))z], \\
v &= -yz(cx + d) + z^2(\beta + \delta y), \\
w &= dz^2/2 + (ca^2 - 2)xz^2/(2a^2) - 2\delta z^3/3,
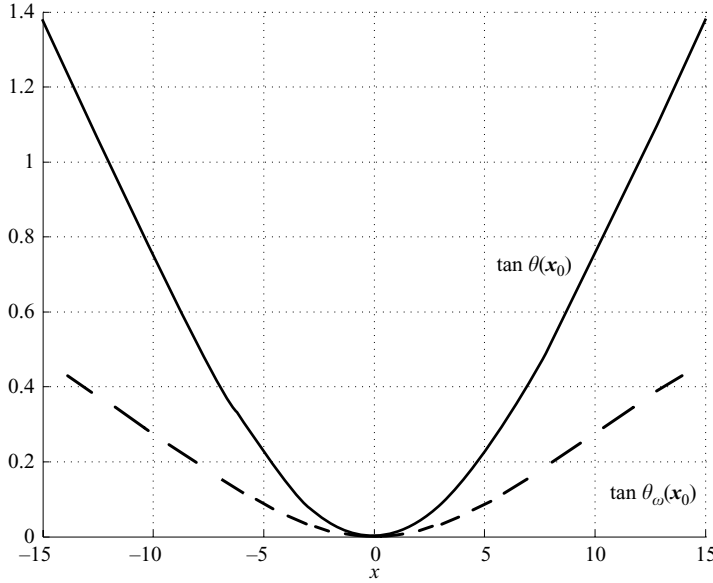\end{aligned}
\right\}
\tag{12.6}
$$

FIGURE 16. Separation bubble model with $a = c = 1$, $b = 10$, $d = 0.5$, $\alpha = 1$, $\beta = 0$, $\delta = -1$. (*a*) Skin-friction trajectories. (*b*) Exact separation line (solid) and its vorticity-based prediction (dashed), the ridge of the scalar field φ. The contours of φ are shown over the region where (E 4) holds. (*c*) Linear prediction for the separation surface by our exact theory; also shown are nearby streamlines.

Separation lines in this example must therefore contain skin-friction trajectories that are backward-asymptotic to p_1 or p_2 and forward-asymptotic to p_3 or p_4. The upper and lower components of the unstable manifold $W^u(p_1)$ satisfy this requirement, yielding a single separation line γ connecting the upper and lower spirals through the saddle p_1.

Figure 16(*b*) compares γ with the prediction of the vorticity-based separation theory. While the vorticity-based prediction is again correct at skin-friction zeros, it suggests a separation line radically different from γ. The numerical simulations in figure 16(*c*) confirm that γ is the correct separation line, and (10.6) is the correct separation slope, which we obtained along γ numerically.

12.6. *Example IV: Open separation along a limit cycle*

In Appendix D, we derive the model velocity field

$$
\left.
\begin{aligned}
u &= \mu xz + yz - x^3z + 8z^3x/3 - xy^2z, \\
v &= -xz + \mu yz - x^2yz - y^3z + 8yz^3/3, \\
w &= -\mu z^2 + 2z^2x^2 + 2z^2y^2 - 4z^4/3,
\end{aligned}
\right\}
\tag{12.8}
$$

with the skin friction field

$$
\boldsymbol{\tau} = \begin{pmatrix} \mu x + y - x^3 - xy^2 \\ -x + \mu y - yx^2 - y^3 \end{pmatrix}.
$$

In this example, $\boldsymbol{p} = (0,0)$ is the only skin-friction zero; at this point, we have

$$
\det \nabla_x \boldsymbol{\tau}(\boldsymbol{p}) = \mu^2 + 1 > 0, \qquad \nabla_x \cdot \boldsymbol{\tau}(\boldsymbol{p}) = 2\mu, \qquad \partial_z^2 w(\boldsymbol{p}, 0) = -\nabla_x \cdot \boldsymbol{\tau}(\boldsymbol{p}) = -2\mu,
$$

thus, by (4.5)–(4.6), $\boldsymbol{p}$ is a separation point for $\mu < 0$ and a reattachment point for $\mu > 0$.

As μ is varied from negative to positive values, an attracting limit cycle Γ emerges at $x^2 + y^2 = \mu$ (figure 17a). This can be verified explicitly by transforming the velocity field to polar coordinates.

The limit cycle Γ satisfies

$$
\int_\Gamma \frac{\boldsymbol{\omega} \cdot ([\nabla_x \boldsymbol{\tau}] \, \boldsymbol{\omega})}{|\boldsymbol{\omega}|^2} \, ds = -2\mu T < 0, \qquad \int_\Gamma \partial_z^2 w \, ds = 4\mu T > 0,
\tag{12.9}
$$

where T is the period of Γ. By (12.9), Γ is non-degenerate (cf. Appendix B) and coincides with a separation line of (S3)-type. Figure 17(b) shows the dashed separation line predicted by the vorticity-based separation theory. In this example, the dashed line is qualitatively correct, but misses the exact location of the limit cycle and is transverse to skin-friction lines.

In order to compute the separation slope, we observe that $\partial_z^2 \boldsymbol{u} \equiv 0$ in the present example. Thus, by formula (10.6), we have

$$
\tan \theta (\boldsymbol{x}_0) = 0,
$$

thus the separation surface is orthogonal to the $z = 0$ plane. By (10.7) and (E 6), the vorticity-based separation theory of Wu *et al.* (2000) also predicts orthogonal separation, but along the incorrect dashed curve of figure 17(b).

Figure 17(c) shows numerically computed streamlines and a higher-order approximation for the separation surface (cf. formula (D 7)), confirming the separation line and slope predicted by our theory.

12.7. *Example V: Model with bifurcating separation patterns*

In Appendix D, §D.6, we derive the model flow

$$
\left.
\begin{aligned}
u &= yz - z^3/6, \\
v &= xz + \mu yz - x^2z + xyz + z^3/3, \\
w &= -(\mu + x)z^2/2,
\end{aligned}
\right\}
\tag{12.10}
$$

with the associated skin-friction field

$$
\boldsymbol{\tau} = \begin{pmatrix} y \\ x + \mu y - x^2 + xy \end{pmatrix}.
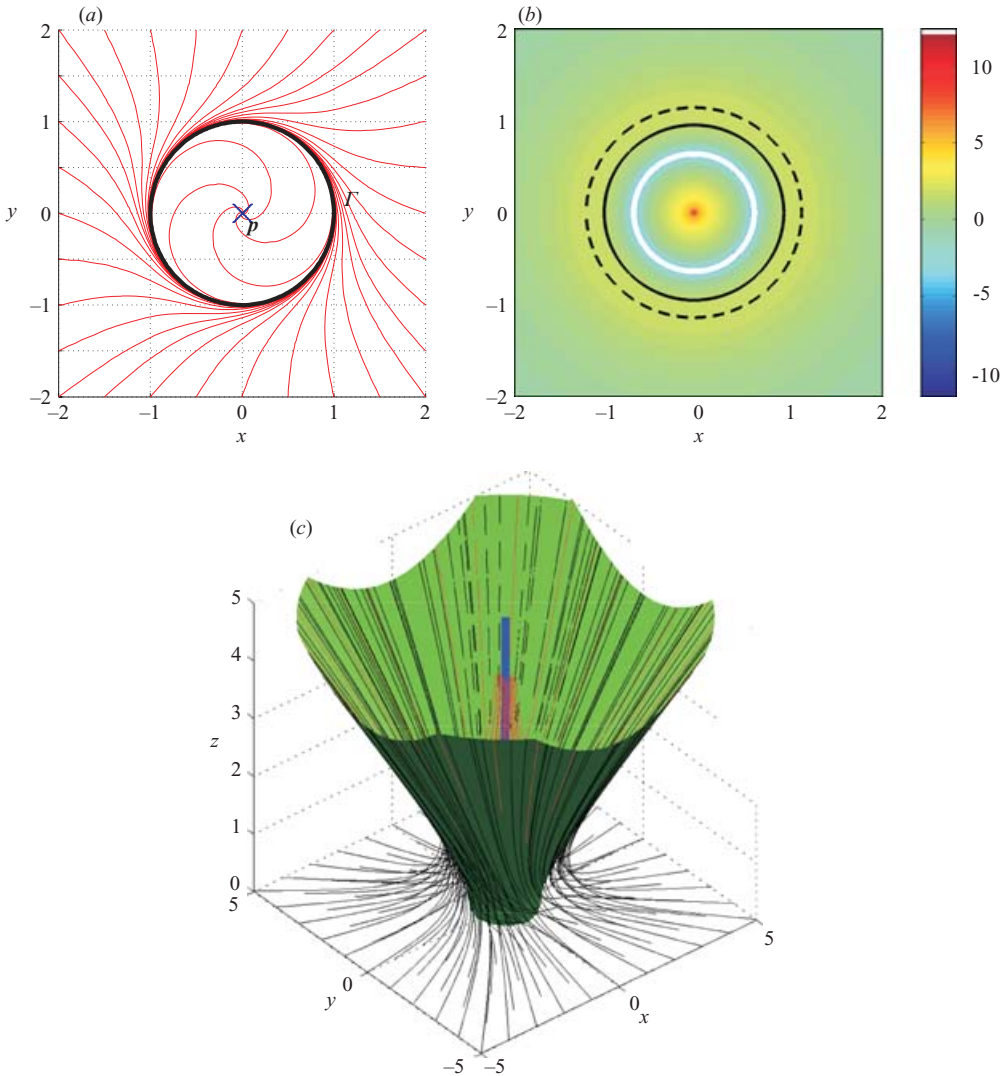$$

FIGURE 17. Open separation model with $\mu = 1$. (*a*) Skin-friction trajectories. (*b*) Exact separation line (solid) and its vorticity-based prediction (dashed), the ridge of the scalar field φ. The contours of φ are shown over the region where (E 4) holds. (*c*) Higher-order prediction for the separation surface by our exact theory; also shown are nearby streamlines.

The fixed points of the $\boldsymbol{\tau}$-field are $\boldsymbol{p}_1 = (0, 0)$ and $\boldsymbol{p}_2 = (1, 0)$. Since

$$\det \nabla_{\boldsymbol{x}} \boldsymbol{\tau}(\boldsymbol{p}_1) = -1, \qquad \partial_z^2 w(\boldsymbol{p}_1, 0) = -\mu, \tag{12.11}$$

the point $\boldsymbol{p}_1$ is a saddle-type skin-friction zero and hence is not a separation point. The point $\boldsymbol{p}_2$ satisfies

$$\det \nabla_{\boldsymbol{x}} \boldsymbol{\tau}(\boldsymbol{p}_2) = 1 > 0, \qquad \nabla_{\boldsymbol{x}} \cdot \boldsymbol{\tau}(\boldsymbol{p}_2) = \mu + 1, \qquad \partial_z^2 w(\boldsymbol{p}_2, 0) = -(\mu + 1), \tag{12.12}$$

thus, by (4.5), $\boldsymbol{p}_2$ is a separation point for $\mu < -1$.

FIGURE 18. (S1) separation in the bifurcating flow model for $\mu = -2$. (*a*) Skin-friction trajectories. (*b*) Exact separation line (solid) and its vorticity-based prediction (dashed), the ridge of the scalar field φ. The contours of φ are shown over the region where (E 4) holds. (*c*) Linear prediction for the separation surface near the wall; also shown are nearby streamlines.

A linear stability analysis shows that p_2 is a stable spiral for $-3 < \mu < -1$, and a stable node for $\mu < -3$. We show the corresponding skin-friction lines in figures 18(*a*) and 19(*a*). By (12.11) and (12.12), the bounded branch of $W^u(p_1)$ satisfies the non-degeneracy conditions for (S1) and (S2) separation for $\mu < -1$. By figure 19(*a*), $W^u(p_1)$ is also tangent to the direction of weaker decay at the node, as required for (S2) separation.

For $\mu > -1$, p_2 becomes an unstable spiral encircled by a stable limit cycle Γ, which is connected to the saddle p_1 by the bounded branch of the unstable manifold $W^u(p_1)$ (see figure 20*a*). The non-degeneracy of the limit cycle can be verified numerically:
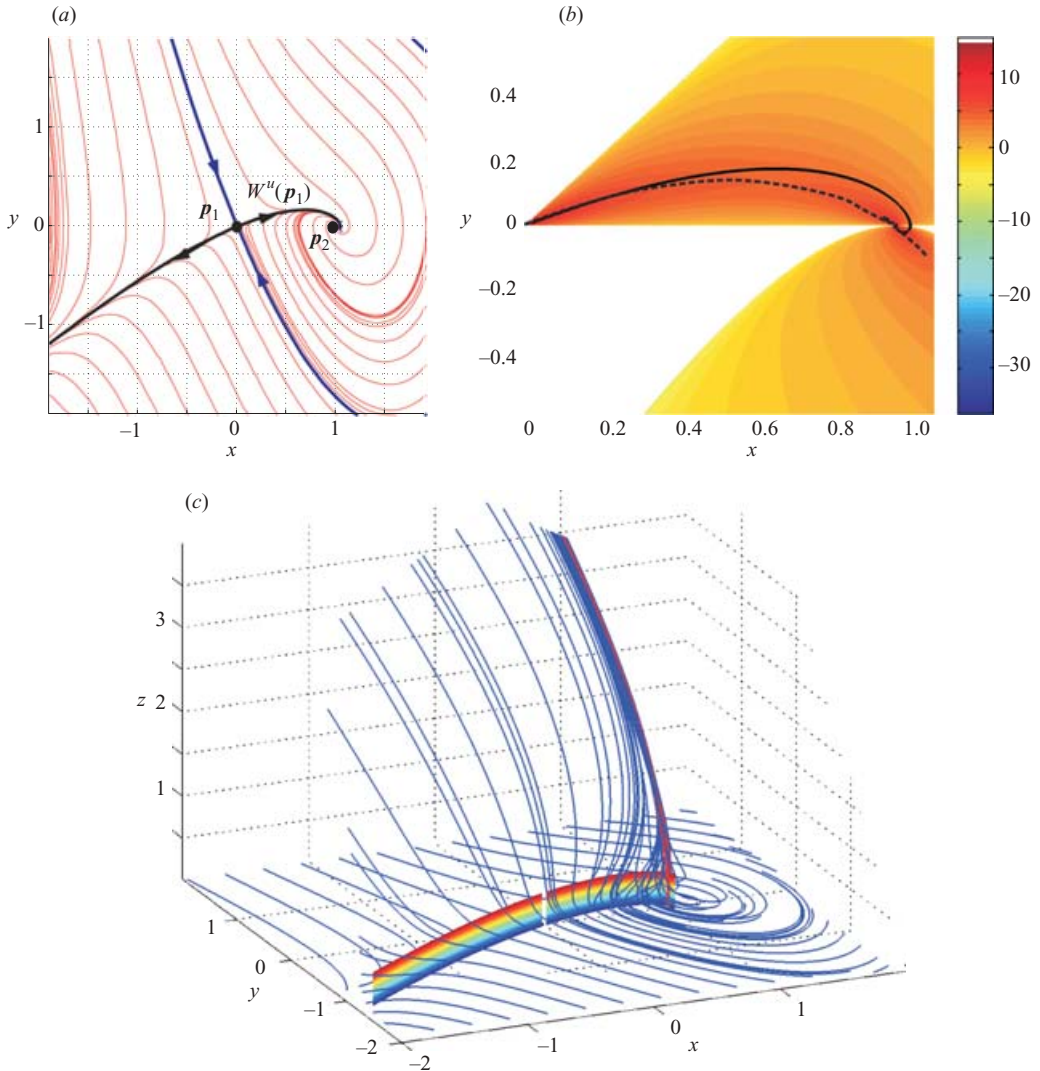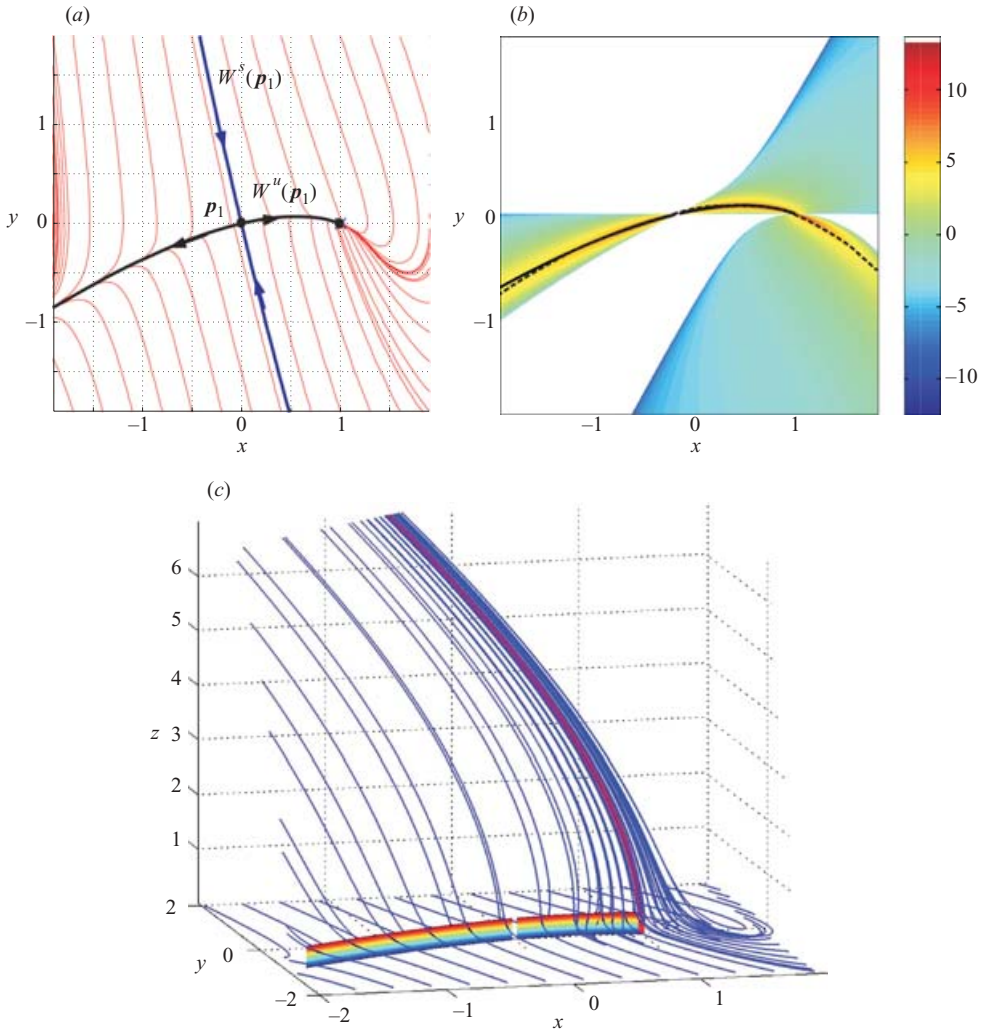
FIGURE 19. (S2) separation in the bifurcating flow model for $\mu = -4$. (*a*) Skin-friction trajectories. (*b*) Exact separation line (solid) and its vorticity-based prediction (dashed), the ridge of the scalar field φ. The contours of φ are shown over the region where (E 4) holds. (*c*) Linear prediction for the separation surface near the wall; also shown are nearby streamlines.

for instance, for $\mu = -0.95$, we obtain

$$\int_{\Gamma} \frac{\boldsymbol{\omega} \cdot ([\nabla_x \boldsymbol{\tau}] \, \boldsymbol{\omega})}{|\boldsymbol{\omega}|^2} \, \mathrm{d}s = -0.42 < 0, \qquad \int_{\Gamma} \partial_z^2 w \, \mathrm{d}s = 0.42 > 0,$$

thus conditions (B 8) and (B 9) are satisfied.

Figures 18(*b*), 19(*b*) and 20(*b*) show the dashed separation line predicted by the vorticity-based theory of Wu *et al.* (2000). In the first two cases, the vorticity-based prediction remains close to the exact separation line owing to the small distance between $\boldsymbol{p}_1$ and $\boldsymbol{p}_2$. In the third case, the vorticity-based prediction fails both quantitatively and qualitatively: it still suggests a separation line between $\boldsymbol{p}_1$ and $\boldsymbol{p}_2$.
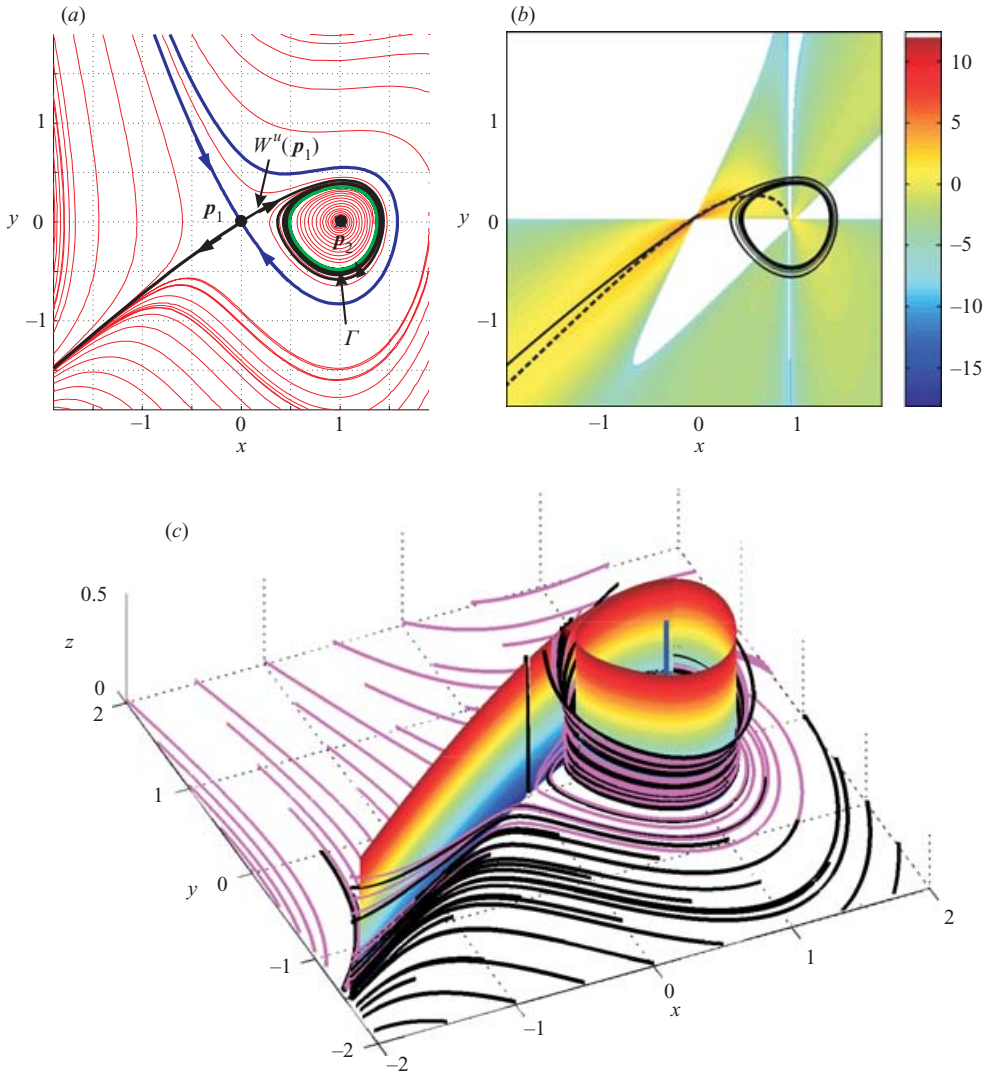
FIGURE 20. (S3) separation in the bifurcating flow model for $\mu = -0.95$. (*a*) Skin-friction trajectories. (*b*) Exact separation line (solid) and its vorticity-based prediction (dashed), the ridge of the scalar field φ. The contours of φ are shown over the region where (E4) holds. (*c*) Linear prediction for the separation surface by our exact theory; also shown are nearby streamlines.

In figure 19(*b*), the separation line predicted by our theory terminates at the skin-friction node $\boldsymbol{p}_2$. By contrast, the vorticity-based prediction continues through the point $\boldsymbol{p}_2$. Beyond the fact that the latter prediction is not a skin-friction line, there is no unique skin-friction line that could be designated as a separation line beyond $\boldsymbol{p}_2$ (see our related discussion on open separation in §11.1). Instead, separation beyond $\boldsymbol{p}_2$ is best characterized by the one-dimensional separation profile emanating from $\boldsymbol{p}_2$.

Figures 18(*c*), 19(*c*) and 20(*c*) show numerical confirmations of the predictions of our theory, with the separation slope calculated numerically from formula (10.6). As suggested above, figure 19(*f*) shows all streamlines near $\boldsymbol{p}_2$ to converge to the

one-dimensional separation profile (red curve) based at p_2; we computed this profile up to second order from formulae (4.10) and (4.11).

13. Conclusions

We have developed a mathematically exact theory of three-dimensional steady separation using nonlinear dynamical systems methods. Our theory covers smooth compressible flows that are locally mass-preserving along a fixed no-slip boundary. We have also given an extension to separation near corners formed by transverse no-slip boundaries.

Our main result is that physically observable separation surfaces are unstable manifolds for saddle-type zeros or limit cycles of the skin-friction field. We have derived conditions under which such surfaces are guaranteed to emerge from the wall; we have also obtained explicit formulae for the leading-order shape of separation surfaces. For Navier–Stokes flows, our criteria and formulae can all be evaluated using on-wall measurements of skin-friction and pressure.

A consequence of our results is that only four robust separation patterns admit uniquely defined separation lines and surfaces. Two of these patterns have been previously described as closed; the other two – classified as open–closed and open in this paper – have not been described in previous studies.

We have illustrated our criteria and slope formulae on local flow models derived from the Navier–Stokes equations through a Perry–Chong-type expansion. Direct numerical simulations of a cavity and a backward-facing step flow also confirm our results (Surana *et al.* 2005).

As we noted in the Introduction, the detachment of fluid from the boundary may just mark a local separation bubble, but may also signal full boundary-layer separation. Three-dimensional experiments and simulations leave little doubt that boundary-layer separation takes place along two-dimensional unstable manifolds. The only question is whether these manifolds emanate from the wall or from off-wall saddle-type trajectories.

While a rigorous answer to the above question seems beyond reach, we would strongly argue for wall-based unstable manifolds. Such manifolds have footprints in the skin-friction field that are routinely observed in numerical and laboratory experiments on three-dimensional boundary-layer separation (see, e.g. Tobak & Peake 1982; Simpson 1996; Délery 2001). These footprints may, in principle, be far from where the boundary layer actually breaks away, but the two-dimensional asymptotic calculations of Sychev (1972) suggest otherwise (see also Smith 1978 for related initial work in three dimensions). Based on all this, we propose that the criteria developed here are necessary conditions for steady boundary-layer separation.

The work presented here is the first in a three-part study of three-dimensional separation. In a follow-up paper, we show how the Lagrangian approach developed here extends to unsteady flows with a well-defined steady mean component (Surana *et al.* 2006). In such flows, separation surfaces become time-dependent, but the underlying separation lines remain fixed, just as separation points do in unsteady two-dimensional oscillatory flows (Haller 2004; Kilic, Haller & Neishtadt 2005).

In a second follow-up paper, we extend the present approach to unsteady flows with a time-varying mean component (Surana & Haller 2006). If the time scale of the mean component is sufficiently far from that of the oscillatory component, the flow displays moving separation. Moving separation turns out to occur along finite-time unstable manifolds; we locate such manifolds by extending the analysis of Haller (2004) and Kilic *et al.* (2005) to three dimensions.

Steady flows with moving no-slip boundaries cannot be treated by the methods described here. Instead, on passing to a frame co-moving with the boundary, one obtains an unsteady velocity field that can be analysed by the methods of Parts 2 and 3 of this study (Surana *et al.* 2006; Surana & Haller 2006). Under certain conditions, however, the separation points or lines may lie off the moving boundary, and hence are not amenable to our boundary-based invariant manifold approach. Such off-wall separation is discussed by Sears & Tellionis (1975) and Elliott, Smith & Cowley (1983) for the two-dimensional boundary-layer equation with an infinite moving boundary.

Appendix A. Proof of separation-line criterion

We first identify S-type and R-type strong hyperbolicity by analysing the linearization of the scaled flow (2.10) along skin-friction trajectories. We then use invariant manifold theory to deduce the emergence of a robust separation or reattachment surface from strongly hyperbolic trajectories.

A.1. *Linearized scaled flow along a skin-friction trajectory*

The linearized scaled flow (2.10) along a skin-friction trajectory $x(s, x_0)$ satisfies

$$\begin{pmatrix} \xi' \\ \eta' \end{pmatrix} = \begin{pmatrix} \nabla_x A(x(s, x_0), 0) & \partial_z A(x(s, x_0), 0) \\ 0 & C(x(s, x_0), 0) \end{pmatrix} \begin{pmatrix} \xi \\ \eta \end{pmatrix}. \tag{A 1}$$

This linear system immediately yields the solution component

$$\eta(s) = \eta_0 \exp \left(\int_0^s C(x(r; x_0), 0) \, dr \right), \tag{A 2}$$

which enables us to re-write the ξ-component of (A 1) as

$$\xi' = \nabla_x A(x(s; x_0), 0)\xi + \eta_0 \partial_z A(x(s; x_0), 0) \exp \left(\int_0^s C(x(r; x_0), 0) \, dr \right), \tag{A 3}$$

a two-dimensional inhomogeneous system of linear ODEs.

Observing that $A(x(s; x_0), 0)$ is a solution of the homogeneous part of (A 3), we introduce the change of coordinates

$$\xi = T(s)\rho, \qquad T(s) = \left[\frac{A(x(s; x_0), 0)}{|A(x(s; x_0), 0)|}, \frac{A^\perp(x(s; x_0), 0)}{|A^\perp(x(s; x_0), 0)|} \right],$$

$$A^\perp(x(s; x_0), 0) = JA(x(s; x_0)), \qquad J = \begin{pmatrix} 0 & -1 \\ 1 & 0 \end{pmatrix}.$$

This coordinate change transforms (A 3) to the form

$$\rho' = R(s)\rho + \eta_0 T^T(s)\partial_z A(x(s; x_0), 0) \exp \left(\int_0^s C(x(r; x_0), 0) \, dr \right), \tag{A 4}$$

where, as found by Haller & Iacono (2003) in a similar calculation, we have

$$\mathbf{R}(s) = \begin{pmatrix} S_\|(s) & a(s) \\ 0 & S_\perp(s) \end{pmatrix}, \qquad a(s) = \left. \frac{\mathbf{A} \cdot ([\nabla_x \mathbf{A}]\mathbf{A}^\perp - [\nabla_x \mathbf{A}^\perp]\mathbf{A})}{|\mathbf{A}|^2} \right|_{x=x(s,x_0),z=0}, \quad \text{(A 5a)}$$

$$S_\|(s) = \left. \frac{\mathbf{A} \cdot ([\nabla_x \mathbf{A}]\mathbf{A})}{|\mathbf{A}|^2} \right|_{x=x(s,x_0),z=0}, \qquad S_\perp(s) = \left. \frac{\mathbf{A}^\perp \cdot ([\nabla_x \mathbf{A}]\mathbf{A}^\perp)}{|\mathbf{A}^\perp|^2} \right|_{x=x(s,x_0),z=0}. \quad \text{(A 5b)}$$

Because $\mathbf{R}(s)$ is upper diagonal, we can solve (A 4) explicitly to obtain

$$\boldsymbol{\rho}(s) = \boldsymbol{\Psi}(s,0)\boldsymbol{\rho}_0 + \eta_0 \int_{s_0}^s \boldsymbol{\Psi}(s,q)\mathbf{T}^T(q)\partial_z \mathbf{A}(x(q;x_0),0) \exp\left(\int_0^q C(x(r;x_0),0)\,dr \right) dq,$$

with the matrix

$$\boldsymbol{\Psi}(s,s_0) = \begin{pmatrix} \exp\left(\int_{s_0}^s S_\|(r)\,dr \right) & \int_{s_0}^s \exp\left(\int_q^s S_\|(r)\,dr + \int_{s_0}^q S_\perp(r)\,dr \right)a(q)\,dq \\ 0 & \exp\left(\int_0^s S_\perp(r)\,dr \right) \end{pmatrix}.$$

$$\text{(A 6)}$$

Thus, by (A 2) and (A 6), the solution of (A 1) takes the following form in the $(\boldsymbol{\rho}, \eta)$ coordinates:

$$\begin{pmatrix} \boldsymbol{\rho}(s) \\ \eta(s) \end{pmatrix} = \boldsymbol{\Phi}(s) \begin{pmatrix} \boldsymbol{\rho}_0 \\ \eta_0 \end{pmatrix}, \quad \text{(A 7)}$$

with

$$\boldsymbol{\Phi}(s) = \begin{pmatrix} \exp\left(\int_0^s S_\|(r)\,dr \right) & \int_0^s \exp\left(\int_q^s S_\|(r)\,dr + \int_0^q S_\perp(r)\,dr \right)a(q)\,dq & d_1(s) \\ 0 & \exp\left(\int_0^s S_\perp(r)\,dr \right) & d_2(s) \\ 0 & 0 & \exp\left(\int_0^s C(x(r;x_0),0)\,dr \right) \end{pmatrix},$$

$$\begin{pmatrix} d_1(s) \\ d_2(s) \end{pmatrix} = \int_0^s \boldsymbol{\Psi}(s,q)\mathbf{T}^T(q)\partial_z \mathbf{A}(x(q;x_0),0) \exp\left(\int_0^q C(x(r;x_0),0)\,dr \right) dq. \quad \text{(A 8)}$$

For later use, we compute $d_2(s)$ to find

$$d_2(s) = \int_0^s \exp\left(\int_q^s S_\perp(r)\,dr + \int_0^q C(x(r;x_0),0) \right) dr \left. \frac{\partial_z^2 w \cdot \boldsymbol{\omega}}{2|\boldsymbol{\omega}|} \right|_{x=x(q,x_0),z=0} dq. \quad \text{(A 9)}$$

A.2. *Strong S-hyperbolicity of skin-friction trajectories*

Here we give a precise mathematical definition of strong S-hyperbolicity. Strong R-hyperbolicity can be defined similarly by reversing the direction of the rescaled time s.

Consider a skin-friction line γ, and let $x(s;x_0)$ be the skin-friction trajectory starting from $x_0 \in \gamma$ at $s = 0$. We say that γ is *strongly S-hyperbolic* with the stable subbundle $\{\eta = 0\}$ and with an unstable subbundle off the $\{\eta = 0\}$ plane, if the following hold:

(1) For any x_0 and for any solution $(\rho_1(s), \rho_2(s), 0)$ of (A 1) that is initially orthogonal to γ, the solution component $\rho_2(s)$ decays to zero exponentially as $s \to \infty$, and grows exponentially as $s \to -\infty$.
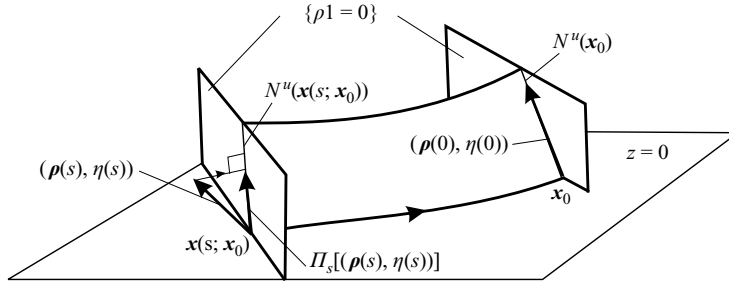
FIGURE 21. Properties of the subspace family $N^u(\cdot)$.

(2) For any x_0, there exists a unique one-dimensional subspace

$$N^u(x_0) = \left\{ k \cdot \left(0, \rho_2^0, \eta^0 \right) \middle| k \in \mathbb{R}, \; \eta^0 > 0, \; \left| \left(0, \rho_2^0, \eta^0 \right) \right| = 1 \right\},$$

such that for any solution $(\rho(s), \eta(s))$ with $(\rho(0), \eta(0)) \in N^u(x_0)$, the orthogonal projection $\Pi_s \left[(\rho(s), \eta(s)) \right]$ of $(\rho(s), \eta(s))$ onto the $\{\rho_1 = 0\}$ plane decays to zero exponentially as $s \to -\infty$ and grows exponentially as $s \to +\infty$.

(3) The subspace family $\text{span}\{N^u(\cdot), (1, 0, 0)\}$ is invariant under the linearized scaled flow, i.e., $\Pi_s \left[\Phi(s) N^u(x_0) \right] \subset N^u \left(x(s; x_0) \right)$ for any $s \in \mathbb{R}$. Furthermore, the angle $\theta \left(x(s; x_0) \right)$ between $N^u \left(x(s; x_0) \right)$ and the normal of the $\{\eta = 0\}$ plane is uniformly bounded for any s (i.e. $N^u \left(x(s; x_0) \right)$ does not approach the $z = 0$ boundary asymptotically).

We show the geometry of properties (2) and (3) in figure 21.

A.3. *Growth and decay rates along skin-friction trajectories*

We now compute all growth and decay rates needed to identify strong S-hyperbolicity. First, we note that by (A 7) and (A 8), property (1) above is equivalent to

$$\limsup_{s \to \infty} \frac{1}{s} \int_0^s S_\perp(r) \, dr < 0, \qquad \limsup_{s \to -\infty} \frac{1}{s} \int_0^s S_\perp(r) \, dr < 0. \tag{A 10}$$

To examine properties (2)–(3), consider a unit vector

$$r^0(x_0) = \begin{pmatrix} 0 \\ \rho_2^0 \\ \eta^0 \end{pmatrix} = \begin{pmatrix} 0 \\ \sin \theta(x_0) \\ \cos \theta(x_0) \end{pmatrix}, \qquad \cos \theta(x_0) > 0,$$

in the $\{\rho_1 = 0\}$ plane. Noting that

$$\Phi(s) r^0(x_0) = \begin{pmatrix} \sin \theta(x_0) \displaystyle\int_0^s \exp \left(\int_q^s S_\parallel(r) \, dr + \int_0^q S_\perp(r) \, dr \right) a(q) \, dq + \cos \theta(x_0) d_1(s) \\[4mm] \sin \theta(x_0) \exp \left(\displaystyle\int_0^s S_\perp(r) \, dr \right) + \cos \theta(x_0) d_2(s) \\[4mm] \cos \theta(x_0) \exp \left(\displaystyle\int_0^s C(x(r; x_0), 0) \right) dr \end{pmatrix}, \tag{A 11}$$

we express property (3) as

$$
\left.
\begin{aligned}
&\left[\sin\theta(\boldsymbol{x}_0)\exp\left(\int_0^s S_\perp(r)\,\mathrm{d}r\right) + \cos\theta(\boldsymbol{x}_0)d_2(s)\right] \\
&\quad = \tan\theta\left(\boldsymbol{x}(s;\boldsymbol{x}_0)\right)\left[\cos\theta(\boldsymbol{x}_0)\exp\left(\int_0^s C(\boldsymbol{x}(r;\boldsymbol{x}_0),0)\,\mathrm{d}r\right)\right], \\
&\qquad \limsup_{s\in\mathbb{R}}|\tan\theta\left(\boldsymbol{x}(s;\boldsymbol{x}_0)\right)| < \infty.
\end{aligned}
\right\}
\tag{A 12}
$$

The orthogonal projection of $\boldsymbol{\Phi}(s)\boldsymbol{r}^0(\boldsymbol{x}_0)$ onto the $\{\rho_1=0\}$ has length

$$
\begin{aligned}
&\sqrt{\left[\sin\theta(\boldsymbol{x}_0)\exp\left(\int_0^s S_\perp(r)\,\mathrm{d}r\right) + \cos\theta(\boldsymbol{x}_0)d_2(s)\right]^2 + \left[\cos\theta(\boldsymbol{x}_0)\exp\left(\int_0^s C(\boldsymbol{x}(r;\boldsymbol{x}_0),0)\,\mathrm{d}r\right)\right]^2} \\
&\quad = \left|\sqrt{1+\tan^2\theta\left(\boldsymbol{x}(s;\boldsymbol{x}_0)\right)}\cos\theta(\boldsymbol{x}_0)\exp\left(\int_0^s C(\boldsymbol{x}(r;\boldsymbol{x}_0),0)\,\mathrm{d}r\right)\right|.
\end{aligned}
\tag{A 13}
$$

Based on (A 7), (A 8), (A 12) and (A 13), properties (2) and (3) can be expressed as

$$
\left.
\begin{aligned}
&\limsup_{s\to-\infty}\frac{1}{s}\log\left[\cos\theta(\boldsymbol{x}_0)\exp\left(\int_0^s C(\boldsymbol{x}(r;\boldsymbol{x}_0),0)\,\mathrm{d}r\right)\right] > 0, \\
&\limsup_{s\to-\infty}\frac{1}{s}\log\left[\sqrt{1+\tan^2\theta\left(\boldsymbol{x}(s;\boldsymbol{x}_0)\right)}\cos\theta(\boldsymbol{x}_0)\exp\left(\int_0^s C(\boldsymbol{x}(r;\boldsymbol{x}_0),0)\,\mathrm{d}r\right)\right] > 0 \\
&\limsup_{s\to\infty}\frac{1}{s}\log\left[\cos\theta(\boldsymbol{x}_0)\exp\left(\int_0^s C(\boldsymbol{x}(r;\boldsymbol{x}_0),0)\,\mathrm{d}r\right)\right] > 0, \\
&\limsup_{s\in\mathbb{R}}|\tan\theta\left(\boldsymbol{x}(s;\boldsymbol{x}_0)\right)| < \infty,
\end{aligned}
\right\}
\tag{A 14}
$$

which is in turn equivalent to the set of conditions

$$
\left.
\begin{aligned}
&\limsup_{s\to-\infty}\frac{1}{s}\int_0^s C(\boldsymbol{x}(r;\boldsymbol{x}_0),0)\,\mathrm{d}r > 0, \\
&\limsup_{s\to\infty}\frac{1}{s}\int_0^s C(\boldsymbol{x}(r;\boldsymbol{x}_0),0)\,\mathrm{d}r > 0, \\
&\limsup_{\boldsymbol{x}_0\in\gamma}|\tan\theta\left(\boldsymbol{x}_0\right)| < \infty.
\end{aligned}
\right\}
\tag{A 15}
$$

A.4. *Separation slope*

We shall now argue that the third condition in (A 15) already follows from (A 10) and from the remaining two conditions in (A 15). As a side result, we obtain an expression for the angle between the separation surface and the local wall normal.

Recall that under conditions (A 15), the second component of $\boldsymbol{\Phi}(s)\boldsymbol{r}^0(\boldsymbol{x}_0)$ decays exponentially to zero as $s\to-\infty$:

$$
\limsup_{s\to-\infty}\frac{1}{s}\log\left|\sin\theta(\boldsymbol{x}_0)\exp\left(\int_0^s S_\perp(r)\,\mathrm{d}r\right) + \cos\theta(\boldsymbol{x}_0)d_2(s)\right| > 0.
\tag{A 16}
$$

Equivalently, for all $s<0$ with large enough $|s|$, we have

$$
0 < K_1 \leqslant \frac{1}{s}\log\left|\sin\theta(\boldsymbol{x}_0)\exp\left(\int_0^s S_\perp(r)\,\mathrm{d}r\right) + \cos\theta(\boldsymbol{x}_0)d_2(s)\right|,
\tag{A 17}
$$

where the constant $K_1 > 0$ can be selected arbitrarily small. For $s < 0$, we can rewrite (A 17) as

$$\frac{\exp^{K_1 s}}{\exp\left(\int_0^s S_\perp(r)\,\mathrm{d}r\right)} \geqslant \left| \sin\theta(\boldsymbol{x}_0) + \cos\theta(\boldsymbol{x}_0) \frac{d_2(s)}{\exp\left(\int_0^s S_\perp(r)\,\mathrm{d}r\right)} \right|.$$

Taking the limit $s \to -\infty$ on both sides of this last inequality, using the second inequality in (A 10), and selecting

$$0 < K_1 < -\limsup_{s\to-\infty} \frac{1}{s}\int_0^s S_\perp(r)\,\mathrm{d}r,$$

we obtain $\tan\theta(\boldsymbol{x}_0) = -\lim_{s\to-\infty}\left[d_2(s)/\exp\int_0^s S_\perp(r)\,\mathrm{d}r\right]$, i.e.

$$\tan\theta(\boldsymbol{x}_0) = \int_{-\infty}^0 \exp\left(\int_0^s [C(\boldsymbol{x}(r;\boldsymbol{x}_0),0) - S_\perp(r)]\,\mathrm{d}r\right) \frac{\partial_z^2 \boldsymbol{u}\cdot\boldsymbol{\omega}}{2|\boldsymbol{\omega}|}\bigg|_{\boldsymbol{x}=\boldsymbol{x}(s,\boldsymbol{x}_0),\ z=0} \,\mathrm{d}s. \quad \text{(A 18)}$$

Now, by the boundedness of $\boldsymbol{x}(s,\boldsymbol{x}_0)$, the second factor in the integrand in (A 18) is uniformly bounded. Also, by the second inequality in (A 10) and by the first inequality in (A 15), the first factor in the integrand in (A 18) decays exponentially in q with an exponent that is uniformly bounded in $\boldsymbol{x}_0$.

From the above, we conclude that (A 18) always gives a $\tan\theta(\boldsymbol{x}_0)$ value that is well-defined and uniformly bounded in $\boldsymbol{x}_0$ whenever the second inequality in (A 10) and the first inequality in (A 15) hold. Selecting the $\theta(\boldsymbol{x}_0)$ defined by (A 18) and proceeding backward through the steps leading from (A 16) to (A 18), we find that the second component of $\boldsymbol{\Phi}(s)\boldsymbol{r}^0(\boldsymbol{x}_0)$ always decays exponentially to zero if the second inequality in (A 10) and the first inequality in (A 15) hold. Thus, the third condition in (A 15) is superfluous.

A.5. Quantitative separation and reattachment criteria

The discussion above implies that the strong S-hyperbolicity conditions in (A 10) and (A 15) can be summarized as

$$\left.\begin{aligned}
&\limsup_{s\to+\infty} \frac{1}{s}\int_0^s S_\perp(r)\,\mathrm{d}r < 0, \quad \limsup_{s\to-\infty} \frac{1}{s}\int_0^s S_\perp(r)\,\mathrm{d}r < 0, \\
&\limsup_{s\to+\infty} \frac{1}{s}\int_0^s C(\boldsymbol{x}(r;\boldsymbol{x}_0),0)\,\mathrm{d}r > 0, \qquad \limsup_{s\to-\infty} \frac{1}{s}\int_0^s C(\boldsymbol{x}(r;\boldsymbol{x}_0),0)\,\mathrm{d}r > 0.
\end{aligned}\right\}$$

(A 19)

With the constants

$$\left.\begin{aligned}
n_+ &= \limsup_{s\to+\infty} \frac{1}{s}\int_0^s S_\perp(r)\,\mathrm{d}r, \quad n_- = \limsup_{s\to-\infty} \frac{1}{s}\int_0^s S_\perp(r)\,\mathrm{d}r, \\
w_+ &= \limsup_{s\to+\infty} \frac{1}{s}\int_0^s C(\boldsymbol{x}(r;\boldsymbol{x}_0),0)\,\mathrm{d}r, \quad w_- = \limsup_{s\to-\infty} \frac{1}{s}\int_0^s C(\boldsymbol{x}(r;\boldsymbol{x}_0),0)\,\mathrm{d}r,
\end{aligned}\right\}$$

the separation conditions (A 19) take the simple form

$$n_{\pm} < 0, \qquad w_{\pm} > 0. \tag{A 20}$$

For reattachment lines, we obtain an analogous criterion by reversing time in all our arguments; this leads to the reattachment conditions

$$n_{\pm} > 0, \qquad w_{\pm} < 0. \tag{A 21}$$

A.6. *Qualitative separation and reattachment criteria*

A.6.1. *Robust separation and reattachment lines*

We recall that the α-limit set of a skin-friction trajectory $x(s; x_0)$ is the set of points visited arbitrarily closely by $x(s; x_0)$ as $s \to -\infty$. The α-limit set is always invariant, i.e. consists of a set of full trajectories. If γ is bounded, then its α-limit set is guaranteed to be non-empty, closed and connected (see, e.g. Guckenheimer & Holmes 1983).

We also recall that the ω-limit set of $x(s; x_0)$ is defined as the α-limit set of $x(-s; x_0)$, i.e. the set of points visited arbitrarily closely by $x(s; x_0)$ as $s \to +\infty$. The properties of ω-limit sets are identical to those listed above for α-limit sets. By the Poincaré–Bendixson theory, the α- and ω-limit set of a bounded planar trajectory is either a fixed point or a set of fixed points connected by skin-friction trajectories or a limit cycle (see, e.g. Guckenheimer & Holmes 1983).

As a consequence, the α-limit set for a strongly S-hyperbolic skin-friction trajectory $x(s; x_0)$ cannot be a stable invariant set because $x(s; x_0)$ approaches the α-limit set in backward time. Furthermore, the α-limit set cannot be an unstable node, unstable spiral, or unstable limit cycle distinct from $x(s; x_0)$; in each such case, $x(s; x_0)$ would attract nearby skin-friction trajectories as $s \to -\infty$.

Therefore, the only possible α-limit set for a bounded strongly S-hyperbolic skin-friction trajectory $x(s; x_0)$ is a saddle-type skin-friction zero or an unstable limit cycle coinciding with $x(s; x_0)$. Both the saddle and the limit cycle must be structurally stable, i.e. robust under small perturbations to the flow (see property (iv) in our requirements for separation in § 3). Saddles and limit cycles are known to be structurally stable if they are *non-degenerate*, i.e. attract nearby skin-friction trajectories at an exponential rate as $s \to -\infty$.

The ω-limit set of a bounded strongly S-hyperbolic skin-friction trajectory $x(s; x_0)$ can only be a stable node, a stable spiral, an attracting limit cycle, or an attracting curve of fixed points with skin-friction trajectories connecting them. For any other ω-limit set, $x(s; x_0)$ would not attract all infinitesimally close trajectories of (2.10) in the $z = 0$ plane.

The last two of the above ω-limit sets – sets of zeros and zeros connected by trajectories – are structurally unstable, i.e. can be dramatically altered by arbitrary small perturbations to the flow. For this reason, we have to exclude them as possible ω-limit sets for a separation line by the robustness requirement (iv) of § 3.

The requirement of robustness also implies the following: if the ω-limit set of a skin-friction trajectory $x(s; x_0)$ in a separation line is a stable node, then the node must have unequal negative eigenvalues and $x(s; x_0)$ must be tangent to the eigenvector corresponding to the larger eigenvalue. Figure 22 shows how equal eigenvalues and tangency to the eigenvector with the smaller eigenvalue leads to a structurally unstable separation line.
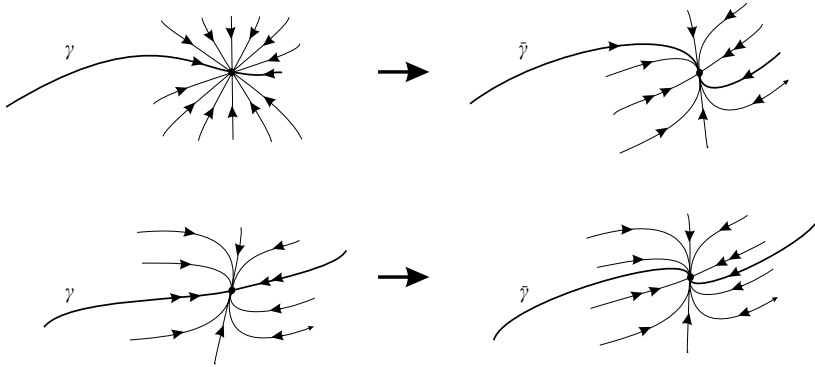
FIGURE 22. The effect of small perturbations on skin-friction lines asymptotic to a degenerate stable node (improper node). Also, the effect of small perturbations on a skin-friction line tangent to the weaker eigenvector of a non-degenerate node (proper node).

The remaining two possible ω-limit sets – stable spirals and stable limit cycles – are structurally stable, as long as they are non-degenerate, i.e. attract nearby skin-friction trajectories at an exponential rate as $s \to \infty$.

Based on the above discussion, the only possible separation lines are those listed in (S1)–(S4) of §6. Reversing the direction of time in our arguments, we obtain that the only possible reattachment lines are those listed in (R1)–(R4) of §6.

A.6.2. *Separation and reattachment surfaces*

Having identified the only possible candidates for separation and reattachment lines, we now give additional conditions under which such candidates are actual separation or reattachment lines, i.e. are contained in separation or reattachment surfaces emanating from the wall.

Conditions on α-limit sets

Assume that the α-limit set of a strongly S-hyperbolic skin-friction trajectory $x(s; x_0)$ is a non-degenerate saddle-type skin-friction zero p. Then p is a saddle-type fixed point for the rescaled flow (2.10) with two eigenvectors in the $z = 0$ plane. The trajectory $x(s; x_0)$ is tangent to the eigenvector corresponding to a positive eigenvalue; the other eigenvector of p – corresponding to a negative eigenvalue – is transverse to γ in the $z = 0$ plane.

Because the trajectory $x(s; x_0)$ is strongly S-hyperbolic, we know that

$$w_- = \limsup_{s \to -\infty} \frac{1}{s} \int_0^s C(x(r; x_0), 0)\, \mathrm{d}r > 0 \tag{A 22}$$

must hold by (A 20). Since $x(s; x_0)$ tends to p exponentially fast in s, we have

$$w_- = \operatorname{sign} C(p, 0) = \operatorname{sign} \partial_z^2 w(p, 0),$$

which, by (A 22), implies

$$\partial_z^2 w(p, 0) > 0. \tag{A 23}$$

Assume now that the α-limit set of a strongly S-hyperbolic $x(s; x_0)$ is a non-degenerate unstable limit cycle that coincides with $x(s; x_0)$. If T denotes the period

of the limit cycle, then the strong S-hyperbolicity condition (A 22) implies

$$w_- = \limsup_{s \to -\infty} \frac{1}{s} \int_0^s C(x(r;x_0),0)\,dr$$

$$= \limsup_{n \to -\infty} \frac{1}{nT}\left[n \int_0^T C(x(r;x_0),0)\,dr \right]$$

$$= \frac{1}{2T}\int_0^T \partial_z^2 w(x(s;x_0),0)\,ds > 0,$$

or, equivalently,

$$\int_\Gamma \partial_z^2 w\,ds > 0. \tag{A 24}$$

Conditions on ω-limit sets

Assume that the ω-limit set of a strongly S-hyperbolic skin-friction trajectory $x(s;x_0)$ is a non-degenerate spiral-type or node-type skin-friction zero q. Then repeating the argument leading to condition (A 23), we find that $w_+ > 0$ implies

$$\partial_z^2 w(q,0) > 0.$$

Assume now that the ω-limit set of a strongly S-hyperbolic $x(s;x_0)$ is a non-degenerate stable limit cycle Γ. Again, repeating the argument leading to (A 24), we find that $w_+ > 0$ implies

$$\int_\Gamma \partial_z^2 w\,ds > 0.$$

Existence of a separation surface

Assume that the α-limit set of a strongly S-hyperbolic skin-friction trajectory $x(s;x_0)$ is a non-degenerate saddle-type skin-friction zero p. We have seen that p must satisfy condition (A 23), which means that the linearized rescaled flow must have a second positive eigenvalue with the corresponding eigenvector off the $z = 0$ plane.

By the stable manifold theorem (see, e.g. Guckenheimer & Holmes 1983), the scaled flow (2.10) has a unique continuously differentiable two-dimensional unstable manifold $W^u(p)$, containing trajectories of (2.10) that are backward-asymptotic to p. $W^u(p)$ is also known to be tangent to the plane $E^u(p)$ spanned by the eigenvectors corresponding to the two positive eigenvalues of the saddle p, see figure 23. Now $x(s;x_0)$ is backward-asymptotic to p, hence $x(s;x_0)$ is contained in $W^u(p)$. But $x(s;x_0)$ is also contained in the invariant plane $z = 0$, thus $W^u(p)$ must intersect the $z = 0$ plane all along $x(s;x_0)$.

Along the intersection, $W^u(p)$ remains transverse to the $z = 0$ plane. Indeed, the linearized flow map of (A 8) is a diffeomorphism, and hence cannot map linearly independent vectors into linearly dependent vectors along $x(s;x_0)$. Also, under the action of the linearized scaled flow (A 1), off-wall vectors tangent to $W^u(p)$ along $x(s;x_0)$ will converge to the off-plane unstable eigenvector of p, and hence remain bounded away from the $z = 0$ plane. Thus, the angle between $W^u(p)$ and the wall normal at x_0 is precisely $\theta(x_0)$, as computed in (A 18). We conclude that $\mathscr{S} = W^u(p)$ satisfies properties (i)–(iv) of a separation surface with slope (A 18).
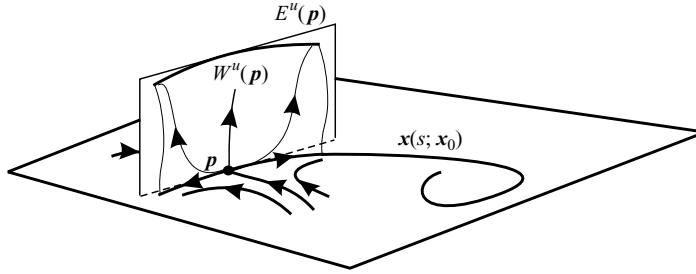
FIGURE 23. The construction of the separation surface as the two-dimensional unstable manifold of the saddle *p*.

Assume now that the α-limit set of a strongly S-hyperbolic skin-friction trajectory $\boldsymbol{x}(s; \boldsymbol{x}_0)$ is a non-degenerate unstable limit cycle Γ that coincides with $\boldsymbol{x}(s; \boldsymbol{x}_0)$. Then condition (A 24) and the formula for (A 8) imply that $\boldsymbol{\Phi}(T)$, the linearized period-T map (Poincaré map) along Γ for the scaled flow, has an eigenvector off the $z=0$ plane with eigenvalue

$$\exp\left(\frac{1}{2}\int_\Gamma \partial_z^2 w \, \mathrm{d}s\right) > 1.$$

Since Γ is a non-degenerate stable limit cycle in the $z=0$ plane, $\boldsymbol{\Phi}(T)$ must also have an eigenvalue of modulus less than one with the corresponding eigenvector transverse to Γ in the $z=0$ plane.

The stable manifold theorem for maps (see, e.g. Guckenheimer & Holmes 1983) then implies the existence of a unique and continuously differentiable one-dimensional unstable manifold for $\boldsymbol{\Phi}(T)$, which means a two-dimensional unstable manifold $W^u(\Gamma)$ for Γ. Again, only vectors tangent to $W^u(\Gamma)$ along Γ remain bounded away from $z=0$ plane in backward time under the linearized flow (A 1). Consequently, the angle between $W^u(\Gamma)$ and the wall normal at $\boldsymbol{x}_0$ is precisely $\theta(\boldsymbol{x}_0)$, as computed in (A 18). We conclude that the surface $\mathscr{S} = W^u(\Gamma)$ satisfies all properties (i)–(iv) of a separation surface with slope (A 18).

The separation criteria (S1)–(S4) of §6 simply summarize the results of this appendix. Reversing the direction of the scaled time s, we obtain the reattachment criteria (R1)–(R4) of §6.

A.7. *Tangential separation is not robust*

The existence of a tangential separation profile is equivalent to the unboundedness of (10.8 *a*). Since the wall-pressure gradient is uniformly bounded in a regular steady Navier–Stokes flow, the first expression in (10.8) can only be unbounded if the matrix

$$-2\nabla_x \boldsymbol{\tau}(\boldsymbol{p}) + \nabla_x \cdot \boldsymbol{\tau}(\boldsymbol{p}) \boldsymbol{I} \tag{A 25}$$

becomes singular. That is the case if and only if $\nabla_x \cdot \boldsymbol{\tau}(\boldsymbol{p})/2$ is a multiplicity-two eigenvalue of the wall-shear Jacobian $\nabla_x \boldsymbol{\tau}(\boldsymbol{p})$.

Out of all possible wall-shear zeros that can generate separation, only non-hyperbolic fixed points and improper stable nodes can have repeated eigenvalues. Non-hyperbolic fixed points, however, will disappear under generic small perturbations. Improper stable nodes do not disappear, but become proper nodes or spirals under small perturbations. As a result, all robust separation profiles must be transverse to the boundary.

The existence of a tangential separation surface is equivalent to the unboundedness of the improper integral in (10.8 *b*). Note, however, that the first factor in this improper integral decays exponentially, and the second factor is uniformly bounded whenever the separation line is bounded. Tangential separation, therefore, could only occur if the separation line started from a non-hyperbolic fixed point or a non-hyperbolic limit cycle of the wall-shear field. Again, such objects are not robust under perturbations.

Appendix B. Non-Degeneracy of separation and reattachment lines

The qualitative conditions (S1)–(S4) and (R1)–(R4) determine four possible separation and four possible reattachment patterns. To identify such patterns in applications, we must also verify the inequalities (A 20) and (A 21), which represent non-degeneracy conditions for the saddles, nodes, spirals, and limit cycles to which the separation lines asymptote. For completeness, we now list the corresponding non-degeneracy conditions for all cases.

We shall use the characteristic equation

$$\lambda^2 - \nabla_x \cdot \boldsymbol{\tau}(\bar{x})\lambda + \det \nabla_x \boldsymbol{\tau}(\bar{x}) = 0 \tag{B 1}$$

associated with the skin-friction Jacobian $\nabla_x \boldsymbol{\tau}(\bar{x})$. We shall also use skin-friction trajectories $x(s)$ that solve the ODE $x' = \boldsymbol{\tau}(x)/(\rho\nu)$. For simplicity, we assume that $\rho\nu = \text{const}$; if that is not the case, $\boldsymbol{\tau}$ should be replaced with $\boldsymbol{\tau}/(\rho\nu)$ in all non-degeneracy conditions listed below.

(S1) $x(s)$ originates from a *saddle* p and ends in a *stable spiral* q.

(*a*) $n_+ < 0$: q attracts nearby skin-friction trajectories at an asymptotic exponential rate if the Jacobian $\nabla_x \boldsymbol{\tau}(p)$ has eigenvalues with negative real parts, i.e. (B 1) has roots with $\text{Re}\,\lambda_i < 0$ for $\bar{x} = q$. That is precisely the case if

$$\nabla_x \cdot \boldsymbol{\tau}(q) < 0, \qquad [\nabla_x \cdot \boldsymbol{\tau}(q)]^2 < 4 \det \nabla_x \boldsymbol{\tau}(q). \tag{B 2}$$

(*b*) $w_+ > 0$: this condition simplifies to $C(q, 0) > 0$, which requires

$$\partial_z^2 w(q, 0) > 0. \tag{B 3}$$

(*c*) $n_- < 0$: this condition holds if p is a non-degenerate saddle, i.e., by (B 1),

$$\det \nabla_x \boldsymbol{\tau}(p) < 0. \tag{B 4}$$

(*d*) $w_- > 0$: this condition simplifies to $C(p, 0) > 0$, which requires

$$\partial_z^2 w(p, 0) > 0. \tag{B 5}$$

(S2) $x(s)$ originates from a *saddle* p and ends in a *stable node* q.

(*a*) $n_+ < 0$: $\nabla_x \boldsymbol{\tau}(q)$ must have unequal negative eigenvalues, i.e. by (B 1), we must have

$$\nabla_x \cdot \boldsymbol{\tau}(q) < 0, \qquad [\nabla_x \cdot \boldsymbol{\tau}(q)]^2 > 4 \det \nabla_x \boldsymbol{\tau}(q). \tag{B 6}$$

(*b*) $w_+ > 0$: same as (B 3).

(*c*) The eigenvector corresponding to the smaller eigenvalue of $\nabla_x \tau(q)$ is

$$e(q) = (-2\partial_y \tau_x(q), 2\partial_x \tau_y(q) - \nabla_x \cdot \tau(q) + \sqrt{[\nabla_x \cdot \tau(q)]^2 - 4\det \nabla_x \tau(q)}).$$

As we discussed earlier (cf. figure 22), $x(s)$ cannot be tangent to $e(q)$, thus we must have

$$e(q) \times \lim_{s \to \infty} \frac{\tau(x(s))}{|\tau(x(s))|} \neq 0. \tag{B 7}$$

    (*d*) $n_- < 0$: same as (B 4).
    (*e*) $w_- > 0$: same as (B 5).
(S3) $x(s)$ originates from a *saddle* p and spirals onto a *stable limit cycle* Γ.

(*a*) $n_+ < 0$: the limit cycle must attract nearby skin-friction trajectories at an exponential rate. That is the case if the average normal strain rate along Γ is negative, i.e. $\int_\Gamma S_\perp(s)\,\mathrm{d}s < 0$. Using the definition of $S_\perp(s)$, we therefore obtain

$$\int_\Gamma \frac{\omega \cdot (\nabla_x [\tau/(\rho\nu)]\,\omega)}{|\omega|^2}\,\mathrm{d}s < 0. \tag{B 8}$$

(*b*) $w_+ > 0$: the limit cycle should be of saddle-type, i.e. must repel nearby off-wall trajectories of the scaled flow (2.10) at an exponential rate. That is the case if the average of $C(x, 0) > 0$ along Γ is positive, i.e.

$$\int_\Gamma \partial_z^2 w\,\mathrm{d}s > 0. \tag{B 9}$$

    (*c*) $n_- < 0$: same as (B 4).
    (*d*) $w_- > 0$: same as (B 5).

(S4) $x(s)$ is a *stable limit cycle* Γ.
    (*a*) $n_+ < 0$: same a (B 8).
    (*b*) $w_+ > 0$: same as (B 9).
    (*c*) $n_- < 0$: holds whenever (B 8) is satisfied ($n_- = n_+$).
    (*d*) $w_- > 0$: holds whenever (B 9) is satisfied ($w_- = w_+$).

The corresponding non-degeneracy conditions for reattachment patterns are obtained from identical arguments in backward time. We only list the results:

(R1) $x(s)$ originates from an *unstable spiral* p and ends in a *saddle* q.

(*a*) $n_- > 0$: equivalent to

$$\nabla_x \cdot \tau(q) > 0, \qquad [\nabla_x \cdot \tau(q)]^2 < 4\det \nabla_x \tau(q). \tag{B 10}$$

(*b*) $w_- < 0$: equivalent to

$$\partial_z^2 w(p, 0) < 0. \tag{B 11}$$

(*c*) $n_+ > 0$: equivalent to

$$\det \nabla_x \tau(q) < 0. \tag{B 12}$$

(*d*) $w_+ < 0$: equivalent to

$$\partial_z^2 w(q, 0) < 0. \tag{B 13}$$

(R2) $x(s)$ originates from an *unstable node* p and ends in a *saddle* q.

    (*a*) $n_- > 0$: equivalent to

$$\nabla_x \cdot \tau(q) > 0, \qquad [\nabla_x \cdot \tau(q)]^2 > 4 \det \nabla_x \tau(q). \tag{B 14}$$

    (*b*) $w_- < 0$: same as (B 11).
    (*c*) With the vector

$$e(p) = (-2\partial_y \tau_x(p), \; 2\partial_x \tau_y(p) - \nabla_x \cdot \tau(p) - \sqrt{[\nabla_x \cdot \tau(p)]^2 - 4 \det \nabla_x \tau(p)}),$$

    we must have

$$e(p) \times \lim_{s \to -\infty} \frac{\tau(x(s))}{|\tau(x(s))|} \neq 0. \tag{B 15}$$

    (*d*) $n_+ > 0$: same as (B 12).
    (*e*) $w_+ > 0$: same a (B 13).

(R3) $x(s)$ spirals off an *unstable limit cycle* Γ and ends in a *saddle* q.

    (*a*) $n_- > 0$: equivalent to

$$\int_\Gamma \frac{\omega \cdot (\nabla_x [\tau/(\rho \nu)] \, \omega)}{|\omega|^2} \, \mathrm{d}s > 0. \tag{B 16}$$

    (*b*) $w_- < 0$: equivalent to

$$\int_\Gamma \partial_z^2 w \, \mathrm{d}s < 0. \tag{B 17}$$

    (*c*) $n_+ > 0$: same as (B 12).
    (*d*) $w_+ > 0$: same a (B 13).

(R4) $x(s)$ is an *unstable limit cycle* Γ.

    (*a*) $n_- > 0$: same as (B 16).
    (*b*) $w_- < 0$: same as (B 17).
    (*c*) $n_+ > 0$: holds whenever (B 16) is satisfied.
    (*d*) $w_+ > 0$: holds whenever (B 17) is satisfied.

Appendix C. Separation slope on curved boundaries

Let $F : (x, z) \mapsto (x, z - f(x))$ denote the map describing the coordinate change $(x, z) \mapsto (x, \tilde{z})$. Vectors based at $(x_0, f(x_0))$ are then carried forward by the derivative map

$$\nabla F^0 = \begin{pmatrix} I & 0 \\ -\nabla_x f(x_0) & 1 \end{pmatrix}$$

to their transformed versions based at $(x_0, 0)$. Specifically, vectors in the tangent space $T_{(x_0, f(x_0))}\mathscr{S}$ of the original separation surface $\mathscr{S}$ at $(x_0, f(x_0))$ are mapped by ∇F^0 into vectors in the tangent space $T_{(x_0, 0)}\tilde{\mathscr{S}}$ of the transformed separation surface $\tilde{\mathscr{S}}$ at $(x_0, 0)$ (see figure 24).

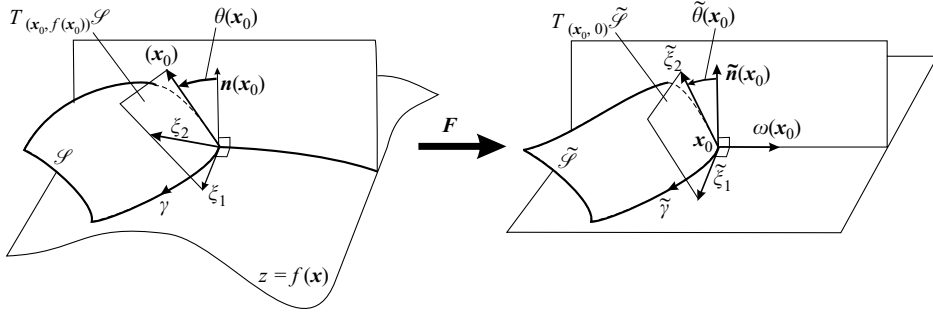FIGURE 24. Local geometry near a point $(\boldsymbol{x}_0, f(\boldsymbol{x}_0))$ of the separation line γ on the curved surface $z = f(\boldsymbol{x})$.

If $\tan \tilde{\theta}(\boldsymbol{x}_0)$ is the separation slope computed from formula (7.1) in the $(\tilde{\boldsymbol{x}}, z)$ coordinates, then the vectors

$$\tilde{\boldsymbol{\xi}}_1 = \begin{pmatrix} \boldsymbol{\tau}(\boldsymbol{x}_0) \\ 0 \end{pmatrix}, \qquad \tilde{\boldsymbol{\xi}}_2 = \begin{pmatrix} \boldsymbol{\omega}(\boldsymbol{x}_0) \tan \tilde{\theta}(\boldsymbol{x}_0) \\ |\boldsymbol{\omega}(\boldsymbol{x}_0)| \end{pmatrix},$$

are contained in the tangent space $T_{(\boldsymbol{x}_0, 0)}\tilde{\mathscr{S}}$. Therefore, their preimages under $\nabla \boldsymbol{F}^0$,

$$\boldsymbol{\xi}_1 = \begin{pmatrix} \boldsymbol{\tau}(\boldsymbol{x}_0) \\ \nabla_x f(\boldsymbol{x}_0) \cdot \boldsymbol{\tau}(\boldsymbol{x}_0) \end{pmatrix}, \qquad \boldsymbol{\xi}_2 = \begin{pmatrix} \boldsymbol{\omega} \tan \tilde{\theta}(\boldsymbol{x}_0) \\ 1 + \tan \tilde{\theta}(\boldsymbol{x}_0) \nabla_x f(\boldsymbol{x}_0) \cdot \boldsymbol{\omega} \end{pmatrix},$$

are contained in the tangent space $T_{(\boldsymbol{x}_0, f(\boldsymbol{x}_0))}\mathscr{S}$.

The intersection of the normal plane $N_{(\boldsymbol{x}_0, f(\boldsymbol{x}_0))}\gamma$ of the separation line and the tangent space $T_{(\boldsymbol{x}_0, f(\boldsymbol{x}_0))}\mathscr{S}$ is a vector $\boldsymbol{\rho}(\boldsymbol{x}_0)$ that lies in the span of $\boldsymbol{\xi}_1$ and $\boldsymbol{\xi}_2$, and is orthogonal to $\boldsymbol{\xi}_1$. Such a vector is given by

$$\boldsymbol{\rho}(\boldsymbol{x}_0) = -(\boldsymbol{\xi}_1 \cdot \boldsymbol{\xi}_2)\boldsymbol{\xi}_1 + \boldsymbol{\xi}_2.$$

Then the tangent of the true separation angle $\theta(\boldsymbol{x}_0)$ enclosed by $\boldsymbol{\rho}(\boldsymbol{x}_0)$ and the local normal

$$\boldsymbol{n}(\boldsymbol{x}_0) = \begin{pmatrix} -\nabla_x f(\boldsymbol{x}_0) \\ 1 \end{pmatrix}$$

to $\mathscr{S}$ is given by

$$\begin{aligned} \tan \theta(\boldsymbol{x}_0) &= \frac{\sin \theta(\boldsymbol{x}_0)}{\cos \theta(\boldsymbol{x}_0)} = \frac{[(\boldsymbol{n}(\boldsymbol{x}_0) \times \boldsymbol{\rho}(\boldsymbol{x}_0)) \cdot \boldsymbol{\tau}(\boldsymbol{x}_0)/|\boldsymbol{\tau}(\boldsymbol{x}_0)|]/[|\boldsymbol{n}(\boldsymbol{x}_0)| |\boldsymbol{\rho}(\boldsymbol{x}_0)|]}{\boldsymbol{n}(\boldsymbol{x}_0) \cdot \boldsymbol{\rho}(\boldsymbol{x}_0)/[|\boldsymbol{n}(\boldsymbol{x}_0)| |\boldsymbol{\rho}(\boldsymbol{x}_0)|]} \\ &= \frac{[\boldsymbol{n}(\boldsymbol{x}_0) \times \boldsymbol{\rho}(\boldsymbol{x}_0)] \cdot \boldsymbol{\tau}(\boldsymbol{x}_0)}{|\boldsymbol{\tau}(\boldsymbol{x}_0)| [\boldsymbol{n}(\boldsymbol{x}_0) \cdot \boldsymbol{\rho}(\boldsymbol{x}_0)]}. \end{aligned}$$

Appendix D. Flow models
D.1. *The Perry–Chong procedure*

We seek the velocity field $\boldsymbol{u}(\boldsymbol{x}) = (u_1(\boldsymbol{x}), u_2(\boldsymbol{x}), u_3(\boldsymbol{x}))$, with $\boldsymbol{x} \equiv (x_1, x_2, x_3)$, $x_3 > 0$, as a Taylor expansion at the boundary point $\boldsymbol{x} = 0$:

$$u_i = A_i + \sum_{j=1}^{3} A_{ij} x_j + \sum_{j,k=1}^{3} A_{ijk} x_j x_k + \sum_{j,k,l=1}^{3} A_{ijkl} x_j x_k x_l + \sum_{j,k,l,m=1}^{3} A_{ijklm} x_j x_k x_l x_m + \dots,$$

$$(D\,1)$$

with dots referring to terms of higher order. A_i, A_{ij}, A_{ijk}, and A_{ijkl} are symmetric tensors in all their indices except for the first one. The total number of independent coefficients is 105.

Perry & Chong (1986) find relations among $A_{ij...}$ by forcing (D 1) to satisfy the continuity equation (2.3), the no-slip boundary conditions on the boundary $x_3 = 0$, and the vorticity transport equations up to cubic order in x_i. For $\rho = 1 \text{ kg m}^{-1}$, this procedure yields

$$
\left.
\begin{aligned}
&A_{1233} = A_{2133}, \qquad A_{1333} = -2A_{1113} - A_{1223} - A_{2123}, \\[4pt]
&A_{2333} = -A_{2113} - A_{1123} - 2A_{2223}, \qquad A_{11233} = A_{21133}, \\[4pt]
&A_{11333} = -2A_{11113} - A_{11223} - A_{21123}, \qquad A_{12233} = A_{21233} \\[4pt]
&A_{12333} = -2A_{11123} - A_{12223} - A_{21223}, \\[4pt]
&A_{11133} = -\frac{A_{223}A_{13}}{24\nu} - \frac{A_{23}A_{123}}{12\nu} - \frac{A_{13}A_{113}}{24\nu} - \frac{A_{21233} + A_{12233} + A_{13333}}{2}, \\[4pt]
&A_{22333} = -A_{21123} - 2A_{22223} - A_{11223}, \qquad A_{21333} = -A_{21113} - 2A_{21223} - A_{11123}, \\[4pt]
&A_{22233} = -\frac{A_{113}A_{23}}{24\nu} + \frac{A_{13}A_{213}}{12\nu} + \frac{A_{23}A_{223}}{24\nu} - \frac{A_{21133} + A_{11233} + A_{23333}}{2}.
\end{aligned}
\right\} \quad \text{(D 2)}
$$

The above relations – combined with the continuity equations and the no-slip condition on the wall – reduce the total number of unknown coefficients to 29. These remaining coefficients can be determined by prescribing local features of the skin-friction field

$$
\tau_1(x_1, x_2) = a_1 + b_1x_1 + c_1x_2 + d_1x_1^2 + e_1x_1x_2 + f_1x_2^2 + g_1x_1^3 + h_1x_1^2x_2 + i_1x_1x_2^2 + j_1x_2^3
$$
$$
\tau_2(x_1, x_2) = a_2 + b_2x_1 + c_2x_2 + d_2x_1^2 + e_2x_1x_2 + f_2x_2^2 + g_2x_1^3 + h_2x_1^2x_2 + i_2x_1x_2^2 + j_2x_2^3.
$$

Equating $\partial_{x_3}(u_1, u_2)|_{x_3=0}$, with (τ_1, τ_2), we obtain

$$
\left.
\begin{aligned}
&A_{13} = a_1, \qquad A_{113} = \frac{b_1}{2}, \qquad A_{123} = \frac{c_1}{2}, \\[4pt]
&A_{1113} = \frac{d_1}{3}, \qquad A_{1123} = \frac{e_1}{6}, \qquad A_{1223} = \frac{f_1}{3}, \\[4pt]
&A_{11113} = \frac{g_1}{4}, \qquad A_{11123} = \frac{h_1}{12}, \qquad A_{11223} = \frac{i_1}{12}, \qquad A_{12223} = \frac{j_1}{4}, \\[4pt]
&A_{23} = a_2, \qquad A_{213} = \frac{b_2}{2}, \qquad A_{223} = \frac{c_2}{2}, \\[4pt]
&A_{2113} = \frac{d_2}{3}, \qquad A_{2123} = \frac{e_2}{6}, \qquad A_{2223} = \frac{f_2}{3}, \\[4pt]
&A_{21113} = \frac{g_2}{4}, \qquad A_{21123} = \frac{h_2}{12}, \qquad A_{21223} = \frac{i_2}{12}, \qquad A_{22223} = \frac{j_2}{4}.
\end{aligned}
\right\} \quad \text{(D 3)}
$$

This leaves nine free coefficients: A_{133}, A_{233}, A_{2133} A_{1133}, A_{2233}, A_{13333}, A_{21133}, A_{21233} and A_{23333}. By choosing these parameters appropriately, we can create various flow patterns near the boundary.

D.2. *Model with linear skin-friction field*

Consider a linear skin-friction field

$$
\tau_1(x_1, x_2) = a_1 + b_1x_1 + c_1x_2,
$$
$$
\tau_2(x_1, x_2) = a_2 + b_2x_1 + c_2x_2,
$$

which has a unique zero if $b_1 c_2 - b_2 c_1 \neq 0$. By (D 2) and (D 3), we obtain the corresponding velocity field

$$
\left.
\begin{aligned}
u_1 &= a_1 x_3 + b_1 x_1 x_3 + c_1 x_2 x_3 + x_3^2 \left[A_{133} + A_{1133} x_1 + A_{1233} x_2 \right], \\
u_2 &= a_2 x_3 + b_2 x_1 x_3 + c_2 x_2 x_3 + x_3^2 \left[A_{233} + A_{1233} x_1 + A_{2233} x_2 \right], \\
u_3 &= -\frac{b_1 + c_2}{2} x_3^2 - \frac{A_{1133} + A_{2233}}{3} x_3^3,
\end{aligned}
\right\}
\tag{D 4}
$$

with nine free parameters. For simplicity, we take $a_1 = a_2 = 0$, which places the skin-friction zero at the origin. In addition, we let $A_{133} = \alpha$, $A_{233} = \beta$, $A_{1133} = A_{2233} = \delta$ and $A_{1233} = 0$. The parameters α, β, and δ then determine the type and the direction of the separation or reattachment at the point $x_1 = x_2 = 0$.

D.3. *Model with unbounded separatrix in the skin-friction field*

Consider the skin friction field

$$
\begin{aligned}
\tau_1(x_1, x_2) &= a x_1, \\
\tau_2(x_1, x_2) &= -b x_2 + c x_1^2.
\end{aligned}
$$

For $a, b > 0$, this skin-friction field has a unique saddle-type zero at the origin. The unstable manifold of the saddle is the x_2-axis; the stable manifold of the saddle has an unbounded parabola-type shape.

We set A_{133}, A_{2133}, A_{233}, A_{2233}, A_{13333}, A_{21133}, A_{21233} and A_{23333} equal to zero and let $A_{1133} = -d$. Then (D 2)–(D 3) give the velocity field (12.3) with all the remaining coefficients obtained from the equations (D 2)–(D 3).

D.4. *Model with separation bubble*

We now consider a quadratic skin-friction field

$$
\begin{aligned}
\tau_1(x_1, x_2) &= (x_1/a)^2 + (x_2/b)^2 - 1, \\
\tau_2(x_1, x_2) &= -(c x_1 + d) x_2,
\end{aligned}
$$

which has a pair of zeros symmetric to the x_1-axis, and another pair symmetric to the x_2-axis. The first pair of zeros are saddles, whereas the second pair are typically spirals. Such a zero distribution is the typical on-wall signature of a separation bubble.

Using (D 2)–(D 3) and letting $A_{133} = \alpha$, $A_{233} = \beta$, $A_{1133} = A_{2233} = \delta$ and $A_{1233} = 0$, we obtain the corresponding velocity field (12.6).

D.5. *Model with stable limit cycle in the skin-friction field*

Consider the skin friction field

$$
\begin{aligned}
\tau_1(x_1, x_2) &= \mu x_1 + x_2 - x_1^3 - x_1 x_2^2, \\
\tau_2(x_1, x_2) &= -x_1 + \mu x_2 - x_2 x_1^2 - x_2^3.
\end{aligned}
$$

Passing to polar coordinates reveals that for $\mu > 0$, this skin-friction field has an attracting limit cycle at $x_1^2 + x_2^2 = \mu$, which encircles an unstable spiral at the origin. The limit cycle is created in a supercritical Hopf bifurcation as μ is varied from negative to positive values. For simplicity, we choose all remaining free coefficients in (D 2)–(D 3) to be zero, which yields the velocity field (12.8).

As we show in § 12.6, the above example exhibits open separation along the limit cycle, with a separation surface that is orthogonal to the $z = 0$ plane. Exploiting the cylindrical symmetry of the model, we can also find a higher-order approximation to the separation surface as follows.

We transform the velocity field (12.8) to cylindrical coordinates to obtain the rescaled equations of motion

$$\dot{r} = \mu r - r^3 + \tfrac{8}{3}z^2, \quad \dot{\theta} = -1, \quad \dot{z} = -\mu z + 2zr^2 - \tfrac{4}{3}z^3. \tag{D 5}$$

Due to rotational symmetry in θ, the (r, z) subsystem

$$\dot{r} = \mu r - r^3 + \tfrac{8}{3}z^2, \quad \dot{z} = -\mu z + 2zr^2 - \tfrac{4}{3}z^3, \tag{D 6}$$

decouples from the full scaled flow and can be analysed separately.

The limit cycle Γ appears in (D 6) as a saddle-type fixed point $(\bar{r}, \bar{z}) = (\sqrt{\mu}, 0)$. The separation surface emanating from Γ is then the unstable manifold of $(\bar{r}, \bar{z})$, which we seek in the form

$$r = f(z) = \sqrt{\mu} + az^2 + O(z^3). \tag{D 7}$$

Using the invariance of the unstable manifold, we differentiate both sides of (D 7) in time and use (D 6) to obtain

$$f(z) = \sqrt{\mu} + \frac{8}{3(7 - 3\mu)}z^2,$$

which gives

$$x^2 + y^2 - \frac{16\sqrt{\mu}}{3(7 - 3\mu)}z^2 = \mu + O(z^4), \tag{D 8}$$

a quadratic approximation for the separation surface.

D.6. *Model with homoclinic bifurcation in the skin-friction field*

The quadratic skin-friction field

$$\tau_1(x_1, x_2) = x_2,$$
$$\tau_2(x_1, x_2) = x_1 + \mu x_2 - x_1^2 - x_1 x_2,$$

is one of the simplest possible vector fields that admit a homoclinic bifurcation as the parameter μ is varied through zero (see Khalil 2002). The homoclinic bifurcation involves the creation and destruction of an orbit that connects a saddle point at $(x_1, x_2) = (0, 0)$ to itself.

The τ-field also admits another fixed point $(x_1, x_2) = (0, 1)$, which undergoes a supercritical Hopf bifurcation as μ is varied through zero. For a range of parameters, the attracting limit cycle created by the Hopf bifurcation also attracts the unstable manifold of the saddle point, creating a connection between the saddle and the limit cycle. For simplicity, we again choose all remaining free coefficients in (D 2)–(D 3) to be zero, which yields the velocity field (12.10).

Appendix E. Vorticity-based separation theory

Here we summarize the vorticity-based incompressible separation theory of Wu *et al.* (2000). We express their results in our notation for comparison with our theory.

Let $x^\perp(s; x_0)$ be a trajectory of the wall-vorticity field $\omega(x)$. Let $e(s)$ and $n(s)$ be the unit tangent and the unit normal to $x^\perp(s)$ so that

$$e(s) = \frac{A^\perp(x^\perp(s; x_0), 0)}{|A^\perp(x^\perp(s; x_0), 0)|}, \qquad n(s) = \frac{A(x^\perp(s; x_0), 0)}{|A(x^\perp(s; x_0), 0)|}.$$

The curvature $\kappa_2(s)$ of $x^\perp(s; x_0)$ satisfies

$$e' = \kappa_2 n, \tag{E 1}$$

thus,

$$\kappa_2(s) = \left(\frac{\mathrm{d}}{\mathrm{d}s} \frac{A^\perp}{\sqrt{A \cdot A}} \right) \cdot n = \left(\frac{(\nabla_x A^\perp) A^\perp}{\sqrt{A \cdot A}} - \frac{\mathrm{d}/\mathrm{d}s\, A \cdot A}{\sqrt{A \cdot A}^3} A^\perp \right) \cdot \frac{A}{|A(x^\perp(s), 0)|}$$

$$= \frac{A \cdot ([\nabla_x A^\perp] A^\perp)}{\sqrt{A \cdot A}^3} = \frac{A \cdot ([\nabla_x J A]\, A^\perp)}{\sqrt{A \cdot A}^3} = -\frac{A^\perp \cdot ([\nabla_x A]\, A^\perp)}{|A^\perp|^3}.$$

We conclude that at any point x_0,

$$\kappa_2 = -S_\perp / |A|. \tag{E 2}$$

Furthermore, along a skin-friction trajectory $x(s; x_0)$, we have

$$\eta_1(s) = \frac{\mathrm{d}}{\mathrm{d}s} \log |A(x(s; x_0), 0)| = \frac{1}{|A|} \frac{2\mathrm{d}/\mathrm{d}s\, A \cdot A}{2\sqrt{A \cdot A}}$$

$$= \frac{A \cdot ([\nabla_x A]\, A)}{|A|^3},$$

thus at any point x_0, we have

$$\eta_1 = S_\| / |A|. \tag{E 3}$$

Wu *et al.* (2000) require that in a separation zone, skin-friction trajectories should converge and the flow should develop an upwelling. They find that these two requirements are equivalent to

$$\kappa_2 > 0, \qquad \kappa_2 (\kappa_2 - \eta_1) > 0,$$

which, by (E 2) and (E 3), can be rewritten as

$$S_\perp < 0, \qquad S_\perp + S_\| < 0. \tag{E 4}$$

For reattachment lines, the analogous criteria are

$$S_\perp > 0, \qquad S_\perp + S_\| > 0.$$

Wu *et al.* (2000) also propose that in addition to satisfying (E 2)–(E 3), a separation line must also be a local maximizing curve (*ridge*) for the scalar field

$$\varphi = \kappa_2(\kappa_2 - \eta_1) = S_\perp(S_\perp + S_\|)/ |A|^2 = S_\perp(S_\perp + S_\|)/ |\omega|^2,$$

which is the product of the τ-line curvature and the strength of the wall-normal upwelling normalized by the wall-vorticity. Thus, Wu et al. propose that the separation line must be a portion of a skin-friction line satisfying

$$\nabla_x \varphi \cdot \omega = 0, \qquad \omega^T \left[\nabla_x^2 \varphi\right] \omega < 0. \tag{E 5}$$

Wu *et al.* also state that (E 4)–(E 5) may be satisfied over an entire skin-friction line (closed separation) or on part of a skin-friction trajectory (open separation).

Note, however, that unless the φ-field is degenerate, (E 5) defines ridges that are not skin-friction lines. Indeed, along any skin-friction trajectory $x(s; x_0)$,

$$\frac{\mathrm{d}}{\mathrm{d}s} \{\nabla_x \varphi\, (x(s; x_0)) \cdot \omega\, (x(s; x_0))\} = \frac{1}{\rho \nu} \{\omega^T \left[\nabla_x^2 \varphi\right] + (\nabla_x \varphi)^T \left[\nabla_x \omega\right]\} \cdot \tau|_{x(s; x_0)} \neq 0,$$

unless $\boldsymbol{\tau}\left(\boldsymbol{x}(s;\boldsymbol{x}_0)\right) \equiv 0$ *or* $\boldsymbol{\tau}\left(\boldsymbol{x}\right)$ is linear, in which case $\nabla_x^2 \varphi \equiv \boldsymbol{0}$ and $\nabla_x \boldsymbol{\omega} \equiv \boldsymbol{0}$. Thus, away from skin-friction zeros, the trajectories of a non-degenerate skin-friction field do not coincide with the ridges of φ.

We conclude that (E 5) fails to capture either open or closed separation lines unless the $\boldsymbol{\tau}$-field is degenerate. Indeed, the vorticity-based separation theory fails to identify the correct separation line in all of our examples of §12, even though it provides a close approximation near skin-friction zeros. Citing numerical difficulties, Wu *et al.* (2000) were unable to validate (E 5) in their example involving a flow past a prolate spheroid. Nevertheless, their example appears to admit a large near-linear domain for the $\boldsymbol{\tau}$-field, thus an exact numerical evaluation of (E 5) may give a good approximation for the separation line.

Finally, Wu *et al.* (2000) propose that for incompressible Navier–Stokes flows, the separation angle defined in figure 8 satisfies

$$\tan \theta_{\boldsymbol{\omega}}\left(\boldsymbol{x}_0\right) = \left.\frac{\partial_2 p}{|\boldsymbol{\tau}|\left(3\kappa_2 - \eta_1\right)}\right|_{\boldsymbol{x}=\boldsymbol{x}_0,\, z=0}, \qquad (\text{E 6})$$

where ∂_2 denotes the derivative in the direction of $\boldsymbol{\omega}$ and p denotes the pressure. Noting that

$$\partial_2 p = \frac{\left(\nabla_x p, \boldsymbol{\omega}\right)}{|\boldsymbol{\omega}|},$$

and using (E 2)–(E 3), we rewrite (E 6) to obtain

$$\tan \theta_{\boldsymbol{\omega}}\left(\boldsymbol{x}_0\right) = \left.\frac{\nabla_x p \cdot \boldsymbol{\omega}}{|\boldsymbol{\tau}|\left(-3S_\perp - S_\parallel\right)}\right|_{\boldsymbol{x}=\boldsymbol{x}_0, z=0} = -\frac{1}{\rho\nu}\left.\frac{\nabla_x p \cdot \boldsymbol{\omega}}{|\boldsymbol{\omega}|\left(3S_\perp + S_\parallel\right)}\right|_{\boldsymbol{x}=\boldsymbol{x}_0, z=0}. \qquad (\text{E 7})$$

To see the connection between this vorticity-based slope-approximation and the true separation slope $\tan \theta\left(\boldsymbol{x}_0\right)$ obtained in (10.8), assume that $\boldsymbol{x}(s, \boldsymbol{x}_0) \equiv \boldsymbol{x}_0$ holds, i.e. $\boldsymbol{x}_0$ is a zero of the skin-friction field. Then the exact slope formula (10.8) can be evaluated as

$$\tan \theta\left(\boldsymbol{x}_0\right) = \frac{1}{\nu\rho} \int_{-\infty}^0 \exp\left(-\frac{1}{2}\left[3S_\perp\left(\boldsymbol{x}_0\right) + S_\parallel\left(\boldsymbol{x}_0\right)\right]s\right) \frac{\nabla_x p\left(\boldsymbol{x}_0, 0\right) \cdot \boldsymbol{\omega}\left(\boldsymbol{x}_0\right)}{2|\boldsymbol{\omega}\left(\boldsymbol{x}_0\right)|}\, \mathrm{d}s$$

$$= -\frac{1}{\rho\nu}\left.\frac{\nabla_x p \cdot \boldsymbol{\omega}}{|\boldsymbol{\omega}|\left(3S_\perp + S_\parallel\right)}\right|_{\boldsymbol{x}=\boldsymbol{x}_0, z=0} = \tan \theta_{\boldsymbol{\omega}}\left(\boldsymbol{x}_0\right). \qquad (\text{E 8})$$

Thus, $\tan \theta\left(\boldsymbol{x}_0\right)$ and $\tan \theta_{\boldsymbol{\omega}}\left(\boldsymbol{x}_0\right)$ are equal at skin-friction zeros, but differ at other points in non-degenerate fluid flows. Indeed, (10.8) and (E 7) only agree throughout γ if the skin-friction field is linear and $\nabla_x p \cdot \boldsymbol{\omega}/|\boldsymbol{\omega}|$ in constant along γ.

REFERENCES

CHAPMAN, G. T. 1986 Topological classification of flow separation on three-dimensional bodies. *AIAA Paper* 86-0485.

DALLMANN, U. 1983 Topological structures of three-dimensional flow separation. *DFVLR Rep.* 1B, pp. 221–282.

DÉLERY, J. M. 2001 Robert Legendre and Henri Werlé: Toward the elucidation of three-dimensional separation. *Annu. Rev. Fluid Mech.* **33**, 129–154.

ELLIOTT, J. W., SMITH, F. T. & COWLEY, S. J. 1983 Breakdown of boundary layers: (i) on moving surfaces; (ii) in semi-similar unsteady flow; (iii) in fully unsteady flow. *Geophys. Astrophys. Fluid Dyns.* **25**, 77–138.

FENICHEL, N. 1971 Persistence and smoothness of invariant manifolds for the flows. *Ind. Univ. Math. J.* **21**, 193–226.

GUCKENHEIMER, J. & HOLMES, P. J. 1983 *Nonlinear Oscillations, Dynamical Systems, and Bifurcations of Vector Fields.* Springer.

HALLER, G. 2004 Exact theory of unsteady separation for two-dimensional flows. *J. Fluid Mech.* **512**, 257–311.

HALLER, G. & IACONO, R. 2003 Stretching, alignment, and shear in slowly varying velocity fields *Phys. Rev.* E **68**, 056304.

HAN, T. & PATEL, V. C. 1979 Flow separation on a spheroid at incidence. *J. Fluid Mech.* **92**, 643–657.

HARTMAN, P. 1982 *Ordinary Differential Equations.* Birkhäuser.

HSIEH, T. & WANG, K. C. 1996 Three-dimensional separated flow structure over a cylinder with a hemispherical cap. *J. Fluid Mech.* **324**, 83–108.

HUNT, J. C. R., ABELL, C. J., PETERKA, J. A. & WOO, H. 1978 Kinematical studies of the flows around free or surface mounted obstacle; applying topology to flow visualization. *J. Fluid Mech.* **86**, 179–200.

KENWRIGHT, D. N., HENZE, C. & LEVIT, C. 1999 Feature extraction of separation and attachment lines. *IEEE Trans. Vis. Comp. Graph.* **5**, 135–144.

KHALIL, H. K. 2002 *Nonlinear Systems.* Prentice Hall.

KILIC, M. S., HALLER, G. & NEISHTADT, A. 2005 Unsteady fluid flow separation by the method of averaging. *Phys. Fluids* **17**, 067104.

LEGENDRE, R. 1956 Séparation de l'écoulement laminaire tridimensionnel. *La Rech. Aéronaut.* **54**, 3–8.

LIGHTHILL, M. J. 1963 Attachment and separation in three-dimensional flows. In *Laminar Boundary Layer Theory, Sect. II 2.6* (ed. L. Rosenhead), pp. 72–82, Oxford University Press.

PEAKE, D. J. & TOBAK, M. 1981 Topological structure of three-dimensional separated flows. *AIAA Paper.* 81-1260.

PERRY, A. E. & CHONG, M., S. 1986 A series expansion study of the Navier-Stokes equations with applications to three-dimensional separation patterns. *J. Fluid Mech.* **173**, 207–223.

PERRY, A. E. & FAIRLIE, B. D. 1974 Critical points in flow patterns. *Adv. Geophys.* B **18**, 200–215.

PRANDTL, L. 1904 Über Flüssigkeitsbewegung bei sehr kleiner Reibung. In *Verh. III, Int. Math. Kongr., Heidelberg*, 484–491.

SEARS, W. R. & TELLIONIS, D. P. 1975 Boundary-layer separation in unsteady flow. *SIAM J. Appl. Maths* **23**, 215–234.

SHEN, S. F. 1978 Unsteady separation according to the boundary layer equations. *Adv. Appl. Mech.* **13**, 177–220.

SIMPSON, R. L. 1996 Aspects of turbulent boundary layer separation. *Prog. Aerospace Sci.* **32**, 457–521.

SMITH, F. T. 1978 Three-dimensional viscous and inviscid separation of a vortex sheet from a smooth non-slender body. *RAE Tech. Rep.* 78095.

SURANA, A., JACOBS, G. & HALLER, G. 2005 Extraction of separation and reattachment surfaces from 3D steady shear flows. *AIAA J.* (submitted).

SURANA, A., JACOBS, G., GRUNBERG, O. & HALLER, G. 2006 Exact theory of three-dimensional flow-separation. Part 2. Fixed unsteady separation. *J. Fluid Mech.* (to be submitted).

SURANA, A. & HALLER, G. 2006 Exact theory of three-dimensional flow-separation. Part 3. Moving unsteady separation. Preprint.

SYCHEV, V. V. 1978 On laminar separation. *Izv. Akad. Nauk. USSR, Mekh. Zidk. Gaza* **3**, 47–59.

TOBAK, M. & PEAKE D. J. 1982 Topology of three-dimensional separated flows. *Annu. Rev. Fluid Mech.* **14**, 61–85.

VAN DOMMELEN, L. L. & COWLEY, S. J. 1990 On the Lagrangian description of unsteady boundary layer separation. Part 1. General theory. *J. Fluid Mech.* **210**, 593–626.

VAN DOMMELEN, L. L. & SHEN, S. F. 1980 The spontaneous generation of the singularity in a separating laminar boundary layer. *J. Comput. Phys.* **38**, 125–140.

WANG, K. C. 1972 Separation patterns of boundary layer over an inclined body of revolution. *AIAA J.* **10**, 1044–1050.

WANG, K. C. 1974 Boundary layer over a blunt body at high incidence with an open-type separation. *Proc. R. Soc. Lond* A **340**, 33–55.

WANG, K. C. 1983 On the dispute about open separation. *AIAA Paper* 83-0296.

WETZEL, T. G., SIMPSON, R. L. & CHESNAKAS, S. J. 1998 Measurement of three-dimensional cross-flow separation. *AIAA J.* **36**, 557–564.

WU, J. Z., GU, J. W. & WU, J. M. 1987 Steady three-dimensional fluid particle separation from arbitrary smooth surface and formation of free vortex layers. *AIAA Paper* 87-2348.

WU, J. Z., MA, H. Y. & ZHOU, M. D. 2005 *Vorticity and Vortex Dynamics*. Springer.

WU, J. Z., TRAMEL, R. W., ZHU, F. L. & YIN, X. Y. 2000 A vorticity dynamics theory of three-dimensional flow separation. *Phys. Fluids* A **12**, 1932–1954.

YATES, L. A. & CHAPMAN, G. T. 1992 Streamlines, vorticity lines, and vortices around three-dimensional bodies. *AIAA J.* **30**, 1819–1826.